Nonlocal Turbulent Mixing in the Convective Boundary Layer Evaluated from Large-Eddy Simulation

ELIZABETH E. EBERT,* ULRICH SCHUMANN, AND ROLAND B. STULL*

Institute of Atmospheric Physics, Deutsche Forschungsanstalt für Luft- und Raumfahrt (DLR), Oberpfaffenhofen, Federal Republic of Germany

ABSTRACT

Large-eddy simulation is used to simulate quasi-steady state convection in a windless mixed layer over a uniform surface with constant heat flux. Different tracers are injected at each discrete height in the model to track vertical transport of tracers as a function of time. The resulting tracer source and destination information is presented in the form of transilient matrices.

These matrices are asymmetric for time increments on the order of the convective time scale, t_*. They show nonlocal mixing occurring over a range of wavelengths up to the mixed layer depth, some convective overturning, and the loss of nearly all of the surface layer air into thermals. Measurements of transport across finite distances exhibit skewed distributions of vertical transport velocity. The relative importance of upward versus downward transport strongly depends on both height and time, as measured by the fractional transport and mixing lengths in each direction. Process, mass, and heat transport spectra show the relatively minor contribution made by small-size eddies as compared to the medium and large scales. Favorable comparisons of these results with a variety of traditional turbulence statistics exemplify the wealth of turbulence information that is captured within a transilient matrix.

1. Introduction

Turbulent mixing in the atmospheric boundary layer takes place on many scales, with the most vigorous mixing generally associated with buoyant convection. Coherent eddies in the form of narrow updrafts and broad downdrafts can extend most of the depth of the convective boundary layer (CBL). The mixing associated with this type of turbulence is nonlocal; that is, the mixing of air into or out of a region is related to processes occurring outside of the immediate vicinity of that region, in addition to local processes.

Even for the simple case of horizontally homogeneous turbulence over a flat surface in the presence of zero mean wind, the complex structure of turbulent motions over many scales produces transports of momentum, heat, moisture, and pollutants which are not adequately described using simple diffusion theories. This has led to the development of higher-order closure schemes (i.e., Mellor and Yamada 1974; Zeman and Lumley 1976; Chen and Cotton 1983; Finger and Schmidt 1986) and high-resolution large-eddy simu-

lation (LES) models (i.e., Deardorff 1974; Moeng 1984; Nieuwstadt and de Valk 1987; Schumann et al. 1987; Mason and Thompson 1987). The LES approach is especially attractive because it explicitly resolves the important scales of motion through direct integration of the Navier–Stokes equation on a very fine three-dimensional model grid.

The primary goal of the study presented here is to investigate vertical nonlocal turbulent mixing in the convective boundary layer using the large-eddy simulation (LES) model of Schumann et al. (1987). The large-eddy simulation can provide a wealth of knowledge about turbulent mixing behavior which would be impossible to measure directly in the atmospheric boundary layer. This mixing information is important not only in the study of turbulence itself, but also in providing boundary conditions for atmospheric flow on larger scales. However, it is still impractical to implement a LES model for the boundary layer within a numerical weather prediction model or a climate model. Therefore, the knowledge gained from the LES must somehow be translated into a simpler but accurate description of vertical nonlocal turbulent mixing, which is adapted to the coarser horizontal resolution of the large-scale model.

One simple framework for describing nonlocal vertical turbulent mixing is the transilient turbulence theory of Stull (1984). In essence, this theory says that the amount of air that mixes from any source altitude to any destination altitude in a horizontally homoge-

---

* On leave from the Boundary Layer Research Team, Department of Meteorology, University of Wisconsin-Madison.

Corresponding author address: Professor Roland B. Stull, Department of Meteorology, University of Wisconsin, 1225 W. Dayton St., Madison, WI 53706.

---

neous boundary layer can be described by a matrix of mixing coefficients. Although it has been half a decade since the concept was discussed in discrete form by Stull (1984) and Stull and Hasagawa (1984), no measurements of the mixing coefficients in the matrix have yet been made. Instead, indirect estimates of this transilient matrix have been presented based on parameterizations (Stull and Driedonks 1987). Direct measurements of nonlocal mixing matrices in the real atmosphere or even in laboratory tanks are difficult due to the difficulty of injecting a sheet of tracer into an already turbulent boundary layer.

In this study we use LES results to directly determine the transilient mixing coefficients. Large-eddy computer simulations allow one to forecast a turbulent boundary layer up to a quasi-steady state, then insert passive scalar tracers, and continue the simulation while tracking average tracer transport. This latter method, while not perfect because of subgrid approximations, can hopefully capture the most important physics for idealized cases such as the CBL.

The LES approach has been used by Lamb (1978), Moeng and Wyngaard (1984), Fiedler and Moeng (1985), Sun and Chang (1986), Nieuwstadt and de Valk (1987), Chatfield and Brost (1987), and Schumann (1989) to investigate dispersion of passive and interactive scalars originating at specified levels in the CBL. Our approach differs from most of these previous studies in that we simultaneously compute the turbulent mixing for sources at *all* levels in the CBL in order to measure the total (resolvable) nonlocal mixing. Moreover, most previous studies introduced tracers as point or line sources, while we are using plane sources so that the results are functions of vertical coordinate and time only. Plane sources at just two levels were used by Fiedler and Moeng (1985) to mark the top-down and bottom-up contributions to mixing.

The approach used here is rather simple, as sketched in Fig. 1. The forecast of the three-dimensional LES is interrupted after a quasi-steady turbulent state is reached. Every grid box within each layer of the model is filled with a unit amount of tracer, where different tracers correspond to the different layers. For example, tracer number 3 originates only from those cells in grid layer number 3. Thus, each tracer is a marker for the source location of air parcels (Fig. 1a). The forecast then resumes, and tracers are allowed to mix in all directions. Later, after some time interval Δt, the amount of each tracer in each horizontal layer of the model is measured, and the result presented in matrix form, as in Fig. 1b. This matrix gives the fraction of air at each destination layer that came from each source layer—the definition of the transilient matrix.

The transilient matrix, in addition to being useful for predicting boundary layer evolution (i.e., Stull and Driedonks 1987), is a convenient tool for studying the nature of the mixing processes. The statistical properties of the coefficients describe the transport and dispersion,

typical mixing lengths and mixing velocities, the spectrum of eddy sizes, and the asymmetry of the mixing. We can compare the transport from a given level with the transport toward that level. The transilient matrices also contain information on upward and downward mixing processes.

In section 2 we describe the transilient turbulence theory, and in section 3 the large-eddy model is summarized. The resulting transilient matrices and their statistical properties are described in section 4 as they relate to characteristics of the vertical mixing processes. The spectrum of scales of the mixing processes themselves, as well as their associated mass and heat fluxes, are also described. Section 5 investigates the dependency of the mixing at a given time on the timestep used in the transilient model formulation. We compare our results with other concepts in section 6. Finally, a summary and conclusions are presented in section 7. Some technical aspects are reported in the appendices.

2. Transilient turbulence concept

a. Basic framework

Transilient turbulence theory is a nonlocal first-order closure approximation that can be used to describe resolvable-scale vertical mixing when the horizontal turbulence is unresolved (as in many meso-, synoptic-, and climate-scale forecast models with large horizontal grid sizes but smaller vertical sizes). In this approach, a matrix of mixing (transilient) coefficients, $[c_{ij}(t, \Delta t)]$, specifies the percentage of air that arrives within destination layer i from source layer j, during time period Δt. Indices i and j can represent neighboring layers as well as layers that are separated in space. Nonlocal mixing descriptions have had a long history under many different names by many investigators, and is reviewed by Stull (1988a).

The forecast equation for scalar $\langle \Psi \rangle$ is written as a simple matrix multiplication:

$$\langle \Psi_i(t + \Delta t) \rangle = \sum_{j=1}^{n} c_{ij}(t, \Delta t)\langle \Psi_j(t) \rangle \qquad (1)$$

where the angle brackets denote a horizontal average. The transilient coefficients must obey mass conservation

$$\sum_{j=1}^{n} c_{ij} = 1,$$

for each grid box i, and tracer conservation,

$$\sum_{i=1}^{n} c_{ij} = 1,$$

for each tracer j.

The first subscript of the transilient matrix represents the destination layer, and the second represents the source layer, allowing easy interpretation of any tran-
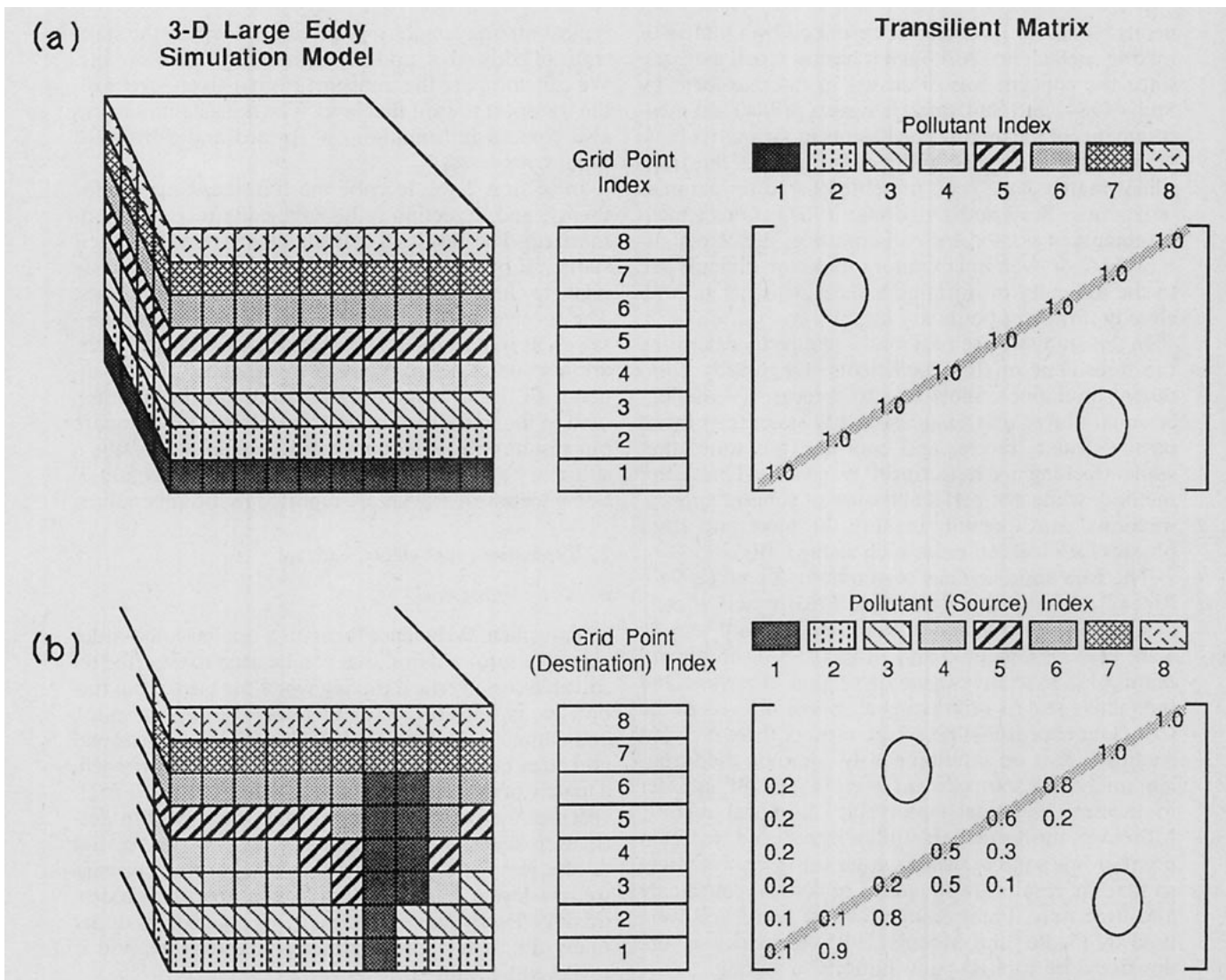
FIG. 1. Schematic diagram showing (a) the initial distribution of tracers with height in a 3-D large-eddy simulation (LES) model, and the corresponding horizontally averaged concentrations represented by the transilient matrix. (b) The same information at a later time after turbulence has transported some of the tracers.

silient matrix (see Fig. 2). The magnitude of an element in the matrix is proportional to the amount of air undergoing mixing, while the distance of the element from the main diagonal is proportional to the size of the eddy. This distance is also related to net advection speed of air parcels, because the matrix applies over a specified timestep, Δt. Elements along the main diagonal of the matrix indicate the fraction of air that remains within a grid box, and hence do not mix outside that box. Such a situation can occur with no turbulence, or with pure subgrid-scale mixing.

Symmetric matrices imply an equal exchange of air between two points (Stull 1984), or isotropy in one dimension (upward mixing equals downward mixing). Asymmetric matrices indicate differing rates of mixing between upward and downward transport (Stull 1988b), or anisotropy in one dimension.

The transilient matrix is a function of both the underlying "physics" (fluid dynamics), and the timestep increment. The physics is often nonstationary as the atmosphere evolves with changing boundary conditions and forcings, making the matrix a function of time. Also, given fixed physics, the total amount of mixing increases as the timestep increases.

The mixing process that causes air from layer j to reach layer i is not directly related to physical eddy size. For example, a series of small physical eddies might contribute to the mixing across a medium distance, given a sufficiently large timestep, while a very large physical eddy might contribute to mixing across the medium distance by partially completing its transport during a short timestep. Similarly, if we employ the concept of air parcels, the mixing from layer j to i might be caused by an air parcel that moved from j to
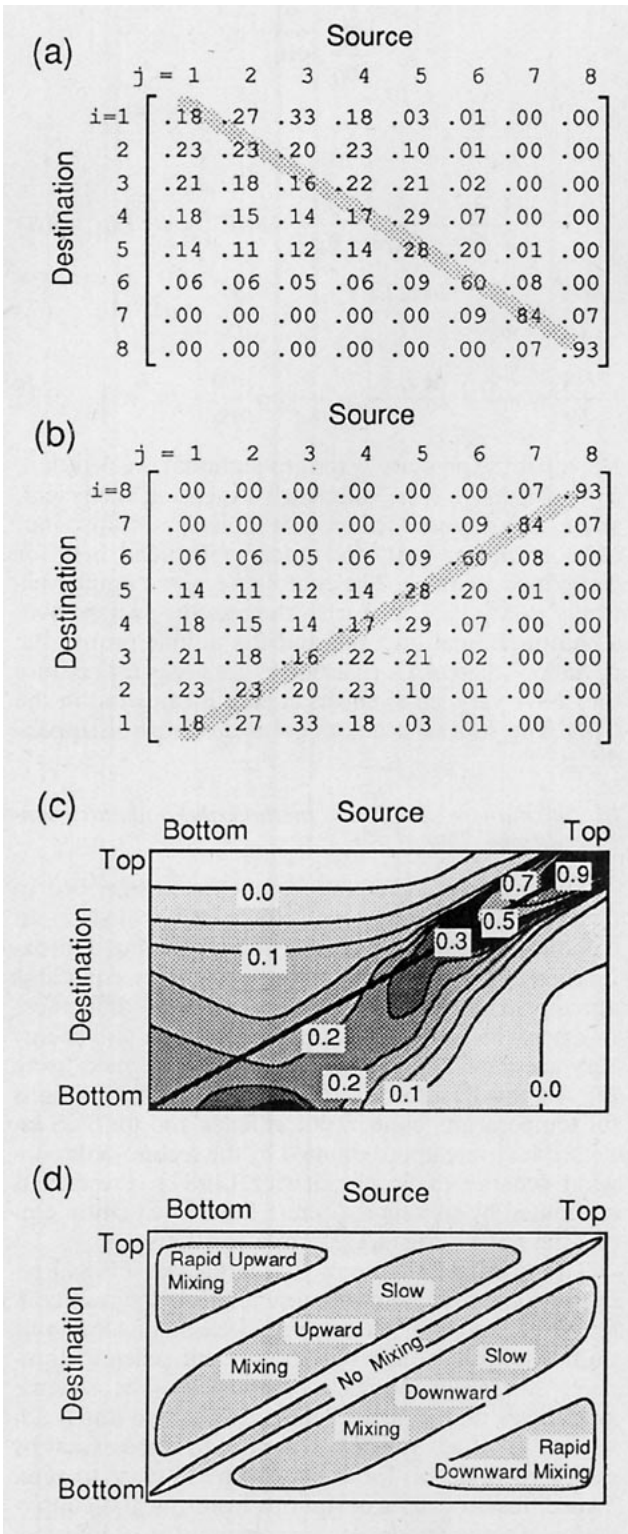
(a)

Source

	j = 1	2	3	4	5	6	7	8
i=1	.18	.27	.33	.18	.03	.01	.00	.00
2	.23	.23	.20	.23	.10	.01	.00	.00
3	.21	.18	.16	.22	.21	.02	.00	.00
4	.18	.15	.14	.17	.29	.07	.00	.00
5	.14	.11	.12	.14	.28	.20	.01	.00
6	.06	.06	.05	.06	.09	.60	.08	.00
7	.00	.00	.00	.00	.00	.09	.84	.07
8	.00	.00	.00	.00	.00	.00	.07	.93

Destination

(b)

Source

	j = 1	2	3	4	5	6	7	8
i=8	.00	.00	.00	.00	.00	.00	.07	.93
7	.00	.00	.00	.00	.00	.09	.84	.07
6	.06	.06	.05	.06	.09	.60	.08	.00
5	.14	.11	.12	.14	.28	.20	.01	.00
4	.18	.15	.14	.17	.29	.07	.00	.00
3	.21	.18	.16	.22	.21	.02	.00	.00
2	.23	.23	.20	.23	.10	.01	.00	.00
1	.18	.27	.33	.18	.03	.01	.00	.00

Destination

(c)

(d)

FIG. 2. Example of an 8 × 8 transilient matrix and its interpretation: (a) given in the standard mathematics format; (b) flipped upside-down to place the origin at the bottom left so that the destination index increases upward, as in typical meteorological presentations; (c) contoured and shaded to highlight regions of strong mixing; and (d) general physical interpretation for any (upside-down) transilient matrix. The main diagonal is highlighted in all figures.

some point well beyond i before returning to layer i during the timestep. We use the words *eddy, eddy size,* and *air parcel* here to refer loosely to the net mixing process between grid points j and i during a time interval, rather than to the physical eddies or to the physical parcel paths.

We can use the transilient concept to examine the kinematic flux of a scalar, and also the contributions from various eddy sizes, called the *transport spectrum.* These quantities are introduced here and will be evaluated in section 4.

b. Kinematic flux

The kinematic flux, F_k, of Ψ across any level, k, that occurs during the time interval between t and $t + \Delta t$ is (Stull 1988c):

$$F_k(t, \Delta t) = \frac{\Delta z}{\Delta t} \sum_{i=1}^{k} \sum_{j=1}^{n} c_{ij} \cdot [\langle \Psi_i(t) \rangle - \langle \Psi_j(t) \rangle] \quad (2)$$

where Δz is the vertical grid spacing, assuming evenly spaced points. If one pictures the grid points to be located in the center of boxes of air, then the fluxes occur between the boxes at levels staggered between the centers of the grid layers (Fig. 3). Hence, air within grid box i is at an average height of $z = (i - 0.5)\Delta z$, and the flux F_i across the top of layer i is at the level $z = i\Delta z$.

One intuitively expects that the flux across any level k should depend only on those eddies that cross that level. We show in appendix A that (2) is mathematically equivalent to
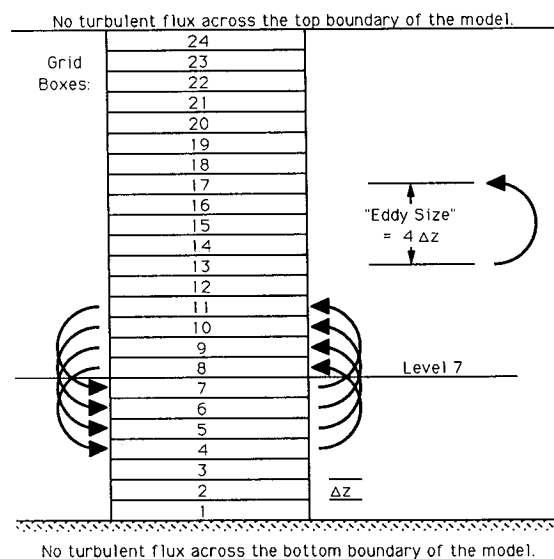

FIG. 3. Schematic showing grid boxes and flux levels. Those mixing processes (eddies) of size $4\Delta z$ that contribute to the flux across level 7 are identified by the arrows.

$$F_k = \frac{\Delta z}{\Delta t} \sum_{i=1}^{k} \sum_{j=k+1}^{n} (c_{ji}\langle \Psi_i \rangle - c_{ij}\langle \Psi_j \rangle) \qquad (3)$$

Remembering that the first subscript of a matrix element always indicates the destination, we see that the first term in (3) describes those eddies or parcels starting at layers below k that carry air of state Ψ_i up towards destination layers above k. Similarly, the second term describes parcels starting above level k and carrying their state Ψ_j to a destination below. Parcels that start and end on the same side of k do not contribute to the flux across that level, as expected (Fig. 3).

c. Transport spectrum

The total flux at any height can be partitioned by eddy size, creating the transport spectrum (Stull 1988d):

$$F_{k|m} = \frac{\Delta z}{\Delta t} \sum_{i=1}^{k} \sum_{j=k+1}^{n} \delta_{m,|i-j|} (c_{ji}\langle \Psi_i \rangle - c_{ij}\langle \Psi_j \rangle) \qquad (4)$$

where $\delta_{m,|i-j|}$ is the Kronecker delta ($\delta_{i,j} = 1$ for $i = j$; $\delta_{i,j} = 0$ otherwise). The term $F_{k|m}$ indicates how much of the flux across level k (at height $k\Delta z$) is associated with eddies of size $m\Delta z$.

The transport spectrum has the same dimensions as a kinematic flux, and exists only when there is transport of a scalar, such as heat. This differs from the classical state spectrum (e.g., Fourier spectrum), which indicates the contribution of various scales to the total variance. Even the state spectrum of flux and the cospectrum of a scalar and velocity do not indicate transport across a distance. The transport spectrum exists when there is mixing across distances.

3. The large-eddy simulation model

The MESOSCOP program, including the LES model used in this paper, has been developed by Schumann et al. (1987). The subgrid scale (SGS) parameterization for momentum and heat transport is fully described in Schmidt and Schumann (1989). Here, we review the changes and additions required for passive scalars.

a. The basic equations

The basic equations describe the mass and momentum budgets and the first law of thermodynamics in terms of grid-averaged velocities, $u_i = (u, v, w)$, temperature, T, and any dynamically passive scalar, Ψ, as a function of the coordinates, $x_i = (x, y, z)$, and of time, t. The Oberbeck–Boussinesq approximation is used; i.e., density, ρ, is assumed to be constant except for buoyancy. In this approximation, temperature T corresponds to the potential temperature in the atmospheric boundary layer (Busse 1978). The budget equations, written in Einstein's summation notation, are

$$\frac{\partial \bar{u}_j}{\partial x_j} = 0, \qquad (5)$$

$$\frac{\partial \bar{u}_i}{\partial t} + \frac{\partial (\bar{u}_j \bar{u}_i)}{\partial x_j}$$
$$= -\frac{1}{\rho}\frac{\partial \bar{p}}{\partial x_i} + \frac{\partial}{\partial x_j}\left(\nu \frac{\partial \bar{u}_i}{\partial x_j} - \overline{u_i'' u_j''}\right) + \beta g \bar{T} \delta_{i3}, \quad (6)$$

$$\frac{D\bar{T}}{Dt} \equiv \frac{\partial \bar{T}}{\partial t} + \frac{\partial (\bar{u}_j \bar{T})}{\partial x_j} = \frac{\partial}{\partial x_j}\left(\mu \frac{\partial \bar{T}}{\partial x_j} - \overline{u_j'' T_j''}\right), \quad (7)$$

$$\frac{D\bar{\Psi}}{Dt} \equiv \frac{\partial \bar{\Psi}}{\partial t} + \frac{\partial (\bar{u}_j \bar{\Psi})}{\partial x_j} = \frac{\partial}{\partial x_j}\left(\gamma \frac{\partial \bar{\Psi}}{\partial x_j} - \overline{u_j'' \Psi''}\right). \quad (8)$$

Here, p is the pressure, g the gravitational acceleration, $\beta = -(\partial \rho / \partial T)/\rho$ the volumetric expansion coefficient, and ν, μ and γ are the constant molecular diffusivities of momentum, heat, and tracers (included here for completeness only). The coordinate $x_3 = z$ points vertically upwards. The overbar denotes the average over a computational grid cell and the double-primes the deviations thereof. Coriolis forces are neglected because they have very small effects at zero mean wind in the CBL. The subgrid scale model is described in appendix B.

b. The numerical solution method and boundary conditions

The numerical integration scheme is described in detail by Schumann et al. (1987). It is based on an equidistant staggered grid and finite difference approximations. The momentum and continuity equations are approximated by second-order central differences in space which conserve mass, momentum and energy very accurately. Time integration is performed using the Adams–Bashforth scheme. The budget equations for temperature, concentration fields and for SGS kinetic energy are approximated by the second-order upwind scheme of Smolarkiewicz (1984). Pressure is computed by solving a discrete Poisson equation employing fast Fourier transform algorithms.

The upwind scheme of Smolarkiewicz (1984) requires some discussion because it affects the results. A first-order upwind scheme would cause unacceptable numerical diffusion, while the present scheme eliminates first-order numerical diffusion. The scheme guarantees that positive fields stay positive under advection. This advantage is balanced to some extent by increased diffusion for fields which are close to zero. This diffusion causes deviations from integral conservation of scalar variance in cases without SGS diffusion, and is discussed in appendix C. If the equations are linear in the advected field, then an arbitrary constant Ψ_0 may be added without changing the mathematical solution. The numerical solution, however, differs because the numerical advection scheme of Smolarkie-

wicz (1984) contains nonlinear approximations and is thus sensitive to this constant as has been noted by Smolarkiewicz and Clark (1986) and Schumann et al. (1987). For the passive scalar fields, the constant is set to 1000 in the reference simulations, but varied in a set of sensitivity tests in appendix C. Before evaluating the results, Ψ_0 is subtracted. The resultant solution may then show small negative spurious oscillations but conserved variance better than if applied with zero Ψ_0.

The computational domain extends horizontally and vertically over a finite domain of size $X \times X \times Z$. At the lateral boundaries, periodicity is assumed. At the top, free-slip boundary conditions are used for the horizontal velocity components, the vertical derivative of potential temperature is prescribed according to the mean potential temperature profile, the vertical diffusive flux of SGS kinetic energy is set to zero, and pressure and vertical velocity are connected by means of the radiation boundary condition of Bougeault (1983) and Klemp and Durran (1983), which reduces the reflection of gravity waves. At the bottom, the imposed heat flux, Q_s, determines the SGS flux at this surface, and the vertical fluxes of horizontal momentum are evaluated from the Monin–Obukhov relationships as described in Schmidt and Schumann (1989). The present study assumes zero surface fluxes of concentration, Ψ.

c. Initial conditions and computational aspects

The initial conditions for potential temperature, velocity and SGS energy are the same as those given in Schmidt and Schumann (1989). The initial potential temperature profile is adiabatic in the mixed layer, and is topped by a layer of uniform lapse rate with constant static stability. Small random temperature and velocity fluctuations in the mixed layer initiate the convective motion. All fields are made nondimensional in terms of a reference inversion height, z_{i0}, and the corresponding convective scales, w_* and T_*, defined by Deardorff (1970). Table 1 gives the values of these parameters. The actual inversion height, z_i, is determined in the simulations as that height where the vertical heat flux assumes its (negative) minimum.

The reference inversion height, z_{i0}, for normalization is that obtained after $6t_*$, where the convective time scale, $t_* = z_{i0}/w_*$, is proportional to the time required for one convection cycle. At this time a quasi-steady

TABLE 1. Values of initial and boundary conditions, and scaling variables in the LES.

Kinematic heat flux from the surface, Q_s	0.06 K m s^{-1}
Convective velocity scale, w_*	1.46 m s^{-1}
Convective temperature scale, T_*	0.041 K
Reference inversion height, z_{i0}	1600 m
Convective time scale, t_*	18.3 min
Brunt–Väisälä frequency in stable layer, N	0.0099 s^{-1}

state of turbulence has been reached. The model is restarted at $t/t_* = 6$ with the previously calculated flow field, but with an injection of tracers into the previously tracer-free forecast. In the remainder of this paper, $t = 0$ refers to this restart time. [A word on notation: the time expressions t/t_* and $\Delta t/t_*$ are equivalent; however, we will use the former when discussing LES results specifically and the latter when discussing quantities derived from the transilient coefficients, $c_{ij}(\Delta t)$.]

The resultant CBL is characterized by a "convective Froude number," $\text{Fr} = w_*/(z_{i0}N) = 0.0922$, where N is the Brunt–Väisälä frequency of the stable layer above the CBL. The surface roughness is set at $z_0 = 10^{-4}z_{i0}$. Molecular diffusivities are effectively zero.

The computational domain extends horizontally over a domain of size $X = 5z_{i0}$ in the x- and y-direction, and vertically from height $z = 0$ to $z = Z = 1.5z_{i0}$. The number of grid cells was varied. Simulations were run for "grid C" (coarse) with $40 \times 40 \times 24$ cells, for "grid M" (medium) with $80 \times 80 \times 24$ cells, and for "grid F" (fine) with $160 \times 160 \times 48$ cells, where the last number counts the grid cells in the vertical direction. The fine grid is the same used by Schmidt and Schumann (1989). Consequently, the grid width varies between $\Delta x = z_{i0}/8$ and $z_{i0}/32$. The timestep is set to $0.004t_*$ for grids C and M, and $0.0025t_*$ for grid F. Grid M was used for most of the calculations presented here (except for some sensitivity tests); thus $\Delta x = \Delta y = \Delta z = 100$ m. The sensitivity of the model results to the grid resolution is discussed in appendix C.

The program is coded such that it can include an arbitrary number of passive scalars. The actual number is limited, however, by the computer resources. For the coarse and medium grids we have used 24 scalar fields to fill each of the 24 grid layers in the model. Only four such fields could reasonably be used with the fine grid on the present computer (CRAY-XMP with 8 million words main storage and up to 64 million words fast secondary storage), and tracers were injected only into a selected subset of the 48 model layers.

In order to compute the $n \times n$ matrix ($n = 24$ for the medium grid) of transilient coefficients, we perform simulations with n scalar fields, Ψ_j. Initially each field is set to zero everywhere except in the j-th grid layer of grids C or M, where it is set to unity. For grid F, which has double the resolution in the vertical direction, the scalar is set to unity in two adjacent grid layers which cover the same height interval as in the coarser grids. (Actually, a constant value, $\Psi_0 = 1000$ is added in the simulations as explained above.)

The horizontal mean values of the results for the concentration, $\langle \Psi_j \rangle$, as a function of vertical grid index, i, at time, Δt, after initialization give approximations to the j-th column of the matrix of transilient coefficients, $[c_{ij}(\Delta t)]$. The results are approximations because of SGS-model errors, finite difference errors,

and because of statistical errors due to the differences between ensemble mean values and horizontal mean values over the finite number of grid points in the computational domain. Note that the numerical approximation errors are probably rather large in the initial period because the concentration distributions start from a Dirac-δ function, which is hard to approximate in any numerical scheme.

d. Resultant concentration and velocity fields

For illustration of the dynamics of the CBL and the induced mixing, Figs. 4a–d show fine-grid results at $t/t_* = 0.2, 0.6$, and 1.0 of three scalar fields starting from different levels, together with the vertical velocity field. The vertical plane selected for display included places where the maximum vertical velocity is reached inside the computational domain. The reduced vertical motions due to the inversion are clearly visible from Fig. 4d. The results illustrate the dominance of resolved eddy transports. The scalar from the lowest level is transported upwards within the main updrafts. "Clean air" from above replaces the "contaminated air" which is drained along the surface towards the plumes. Figure 4b shows that a layer of contaminated air in the middle of the CBL experiences strong upward transport at places with strong updrafts, but is generally advected downwards because of the dominance of areas with sinking fluid. This layer experiences the strongest mixing relative to the two others shown. A pollutant layer near but below the inversion, Fig. 4c, is mainly transported downwards within the downdrafts. Clean air from below displaces the contaminated layer near the inversion. The polluted air comes close to the ground. The results show clearly that the mixing is far from complete in the time interval of $1.0t_*$ for which these results are computed with the fine grid. Therefore, the medium grid was used as a computational expedient, and the model was run out to $t/t_* = 4$.

4. Resulting transilient matrices

Because a different tracer is inserted at each level in the LES, the transilient coefficients $c_{ij}(\Delta t)$ are directly approximated by the horizontal mean values of each scalar concentration, $\langle \Psi_j \rangle$, at vertical grid index, i, at time, Δt, after initialization. In the following discussion the transilient coefficients and scalar concentrations will be treated as equivalent. Thus, the variation of the transilient coefficients in time and space describes the behavior of the simulated convection in a horizontal mean sense. Our results allow us to separate the upward and downward transport processes, as well as transport from and toward each vertical level. Here we examine some statistical properties of the transilient coefficients which reveal the nature of the mean vertical transport, dispersion, asymmetry, and nonlocalness of the mixing.

a. Description of the transilient matrices

Figure 5 shows the 24 × 24 element matrices of transilient coefficients, presented as contour plots, at several time intervals $\Delta t/t_*$ in the grid M simulation. As discussed previously, values of c_{ij} lying below the main diagonal indicate downward transport, and values above the main diagonal indicate upward transport, with greater distances from the main diagonal signifying larger eddy sizes and faster transport.

At small values of $\Delta t/t_*$ the transport is extremely small in both directions. Asymmetry in the transport is evident quite early (Fig. 5b) as the air from the lowest levels begins to be diffused upward. For longer time intervals the majority of the scalar transport is downward as evidenced by the axis of peak concentration values which lies below the main diagonal (Figs. 5c, d, and e). Only the air originating near the surface has moved upward. These results agree with the qualitative picture of scalar transport shown by the instantaneous vertical cross sections shown in Fig. 4, and with the established laboratory results of Willis and Deardorff (1975, 1976, 1981) and numerical CBL simulation of Nieuwstadt and de Valk (1987).

Let us characterize the intermediate timestep matrices in more detail. In particular, we examine $[c_{ij}(\Delta t)]$ at $\Delta t/t_* = 2.0$, which will serve as a reference case for a set of experiments described in section 5.

The reference matrix, $[c_{ij}(2t_*)]$, shows the following characteristics:

(i) *considerable mixing over the whole depth of the mixed layer*, because of the nonzero elements in the lower left $\frac{2}{3}$ of the matrix;

(ii) *most of the air originating near the surface has moved elsewhere* during this long timestep, as indicated by the relative minimum in the lower left corner;

(iii) *convective overturning* is occurring, because of the relatively large values near the ends of the cross-diagonal through the mixed layer (dashed line);

(iv) *asymmetry*, because the ridge of maximum magnitude (dotted line) drops to the lower right of the main diagonal;

(v) both the net transport velocity (distance moved per timestep) and the amount of downward-moving air from within the top third of the mixed layer increase as the destination point approaches the ground, as shown by the distance of the dotted line from the main diagonal, and magnitudes of c_{ij} along the dotted line;

(vi) there are *greater upward transport velocities than downward*, since the 0.01 contour line is farther from the main diagonal for upward transport;

(vii) a *small amount of diffusion in the free atmosphere* above the mixed layer, associated with the numerical problems discussed in section 3b. If there were no diffusion, then all of the elements in the upper third and right third of the matrix would be zero, except for ones along the main diagonal.
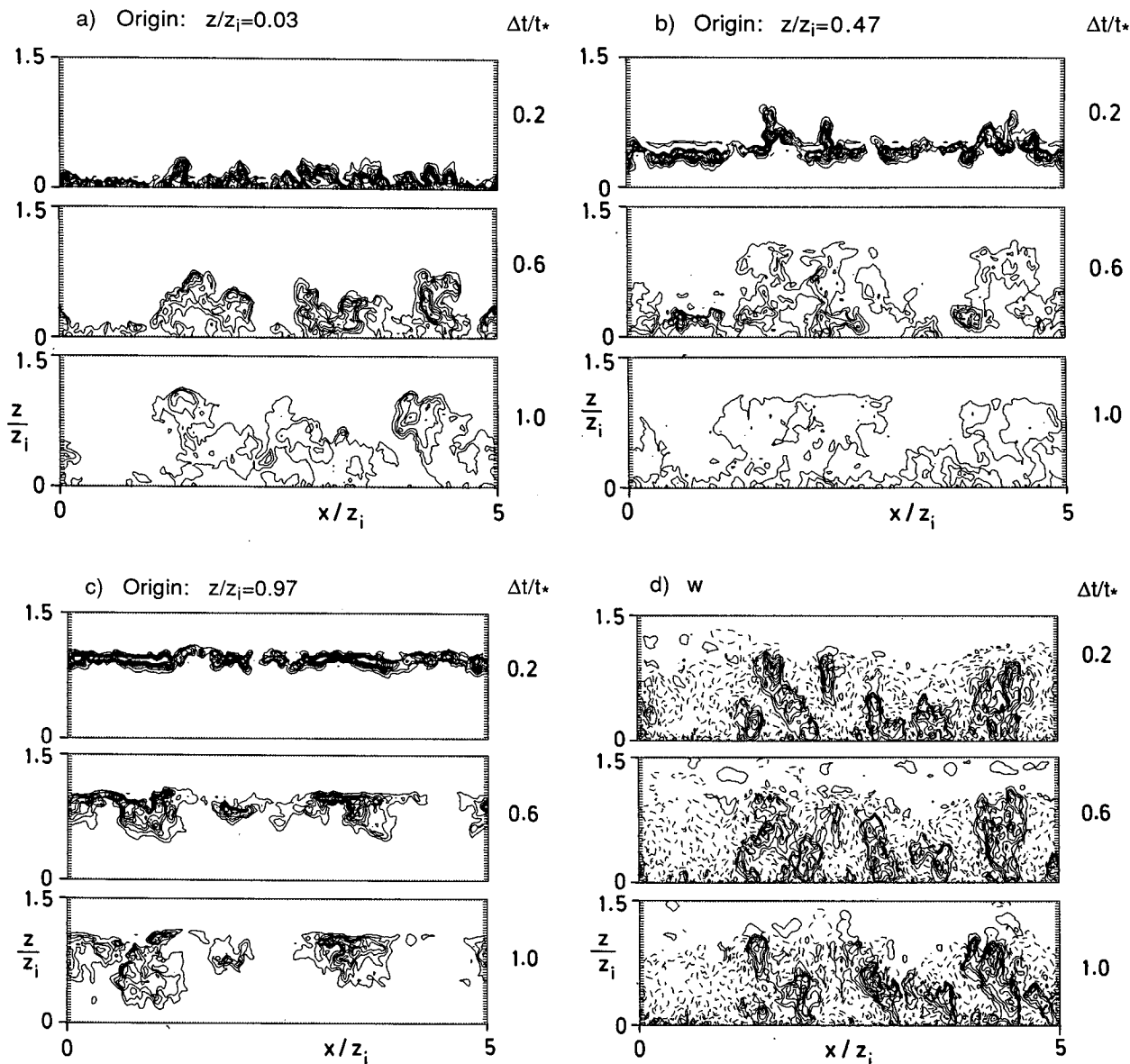
FIG. 4. (a) Scalar concentration at $t/t_* = 0.2$, 0.6, and 1.0 for air originating at $z/z_i = 0.03$. The fine grid LES model was used, and the contour intervals are 0.05, 0.15, 0.25, . . . , 0.95; (b) as in (a), for air originating at $z/z_i = 0.47$; (c) as in (a), for air originating at $z/z_i = 0.97$; (d) vertical velocity field at the same times. The contour interval is 0.3 m s^{-1}, and the dashed contours represent negative velocities.

After several time units the CBL is well mixed and the air originating from each level is distributed more or less uniformly over the entire lower portion of the domain (Fig. 5f). Some diffusion can be seen in the stable layer. While a fraction of this represents physical diffusion, the bulk of it is numerical, resulting from the response of the subgrid scale turbulence parameterization to linear waves generated at the inversion level. We will therefore confine our discussion primarily to the behavior of the coefficients in the mixed layer.

b. Time dependence of mixing

We can follow the time evolution of the vertical mixing of fluid originating at a given level j by examining the values of c_{ij} for the jth column. Figure 6 shows the transilient coefficients as a function of time for four levels in the CBL. Air from near the surface is transported upward in time, with the concentration maximum reaching $0.75z/z_i$ after 1.3 time units, then returning slowly to the middle of the mixed layer. For
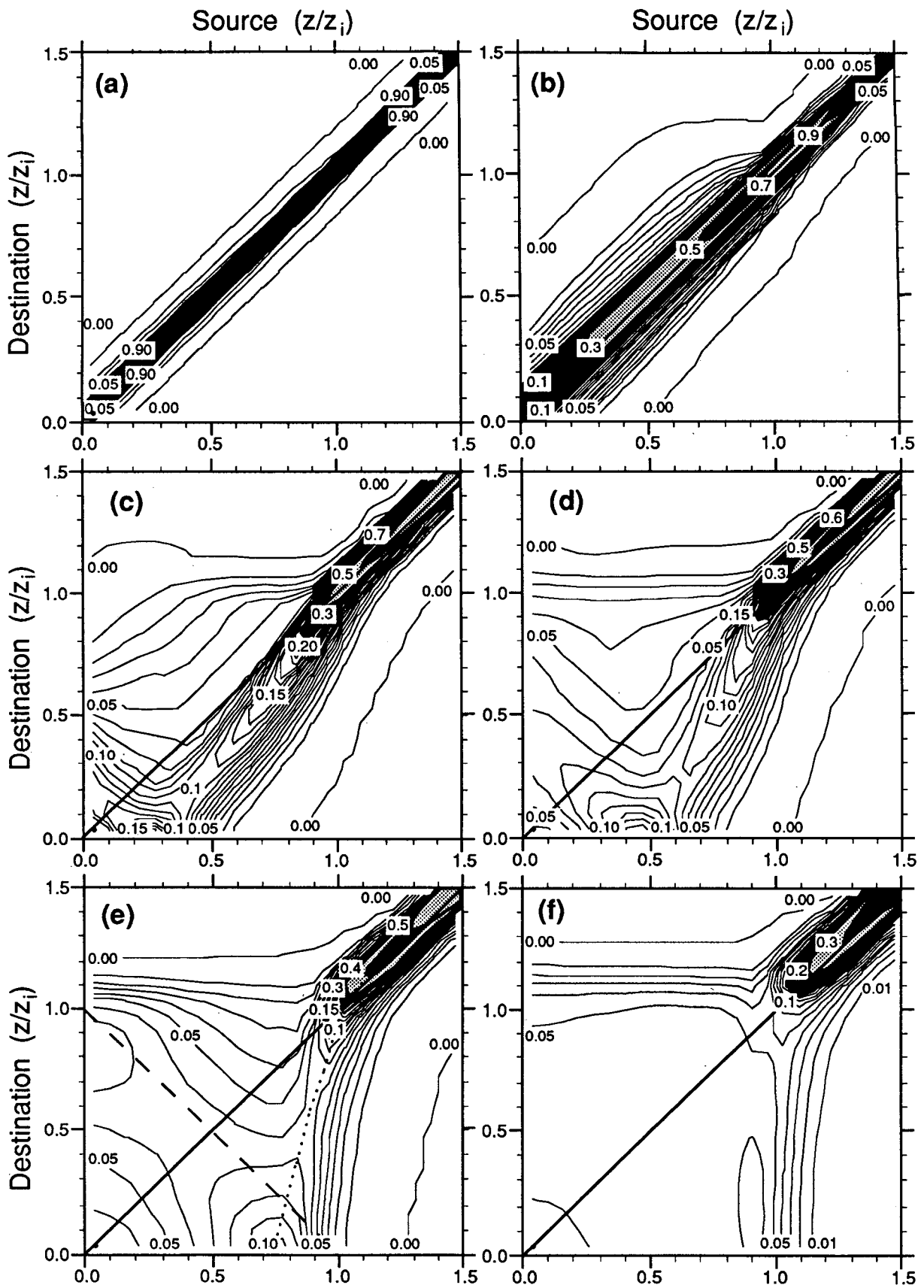
FIG. 5. Contour plots of the transilient matrices at selected time intervals, $\Delta t / t_* =$: (a) 0.02, (b) 0.2, (c) 0.6, (d) 1.0, (e) 2.0, (f) 4.0. The matrices have been turned upside-down so that the lower left corner corresponds to the origin. The contour interval is 0.01, except in the upper right corner.

air originating at $0.22z/z_i$ and $0.47z/z_i$, downward transport occurs for $\Delta t/t_* < 1$, after which the concentration maximum rises toward the middle of the CBL. This same behavior was observed by Willis and Deardorff (1978) in their laboratory tank experiments, and by Eberhard et al. (1988) in the atmospheric CBL during the CONDORS (CONvective Diffusion Observed by Remote Sensors) experiment. Near the inversion level the air is effectively trapped beneath the stable layer, with only a slow upward diffusion of concentration associated with the numerical problem discussed earlier. The net transport is strongly downward; in fact, a weak local maximum in concentration is found at the surface at $\Delta t/t_* \approx 3$. Note that the transport diagrams of Fig. 6 do not have the same meaning as a snapshot of a tracer plume because we are following the dispersion of a layer of tracer rather than of a linear point tracer.

The corresponding vertical fluxes of tracers originating at the same four levels are plotted in Fig. 7. These are obtained as horizontal averages of $\overline{w''\Psi''}$ at various time points in the LES calculation. Initially the vertical tracer fluxes correspond strongly to the tracer gradient, i.e., a large downward flux is associated with a large positive vertical concentration gradient, and vice versa. However, several regions with counter-gradient fluxes develop between $\Delta t/t_* \approx 0.5$ and $\Delta t/t_* \approx 2.0$. For sources near the surface (Figs. 7c, d) the flux continues to be upward at all levels even though the level of maximum concentration rises with time, creating an area of positive concentration gradient below that level. At midlevels a counter-gradient downward flux is seen in an area of negative concentration gradient for $0.5 \leqslant \Delta t/t_* \leqslant 1.0$ (Fig. 7b). For a source near the inversion, the fluxes just below the inversion are against the local gradient for $0.5 \leqslant \Delta t/t_* \leqslant 2.8$ (Fig. 7a). Thus we see that for intermediate time intervals, the mixing cannot be accurately described by simple down-gradient approximations. We shall examine the resulting implications for K-theory later in section 6.

c. Mean vertical transport and dispersion

The mean transport of tracers originating at the jth level after some time interval Δt is obtained by weighting each destination level i by c_{ij} to get the mean position, or center of mass, $\bar{z}_j(\Delta t)$:

$$\bar{z}_j(\Delta t) = -0.5\Delta z + \Delta z \sum_{i=1}^{n} c_{ij}(\Delta t) \cdot i \qquad (9)$$

The mean vertical transport distance is simply $\bar{z}_j(\Delta t)$ $- (j - \frac{1}{2}) \cdot \Delta z$. For tracers originating near the surface, $\bar{z}_j$ is analogous to the mean plume height. When plotted as a function of time (Fig. 8) we see that on average the mean height of tracers originating near the surface rises to about 60% of the depth of the mixed layer before lowering to $0.5z_i$ in the uniformly mixed layer. Conversely, the mean position of tracers from near the in-
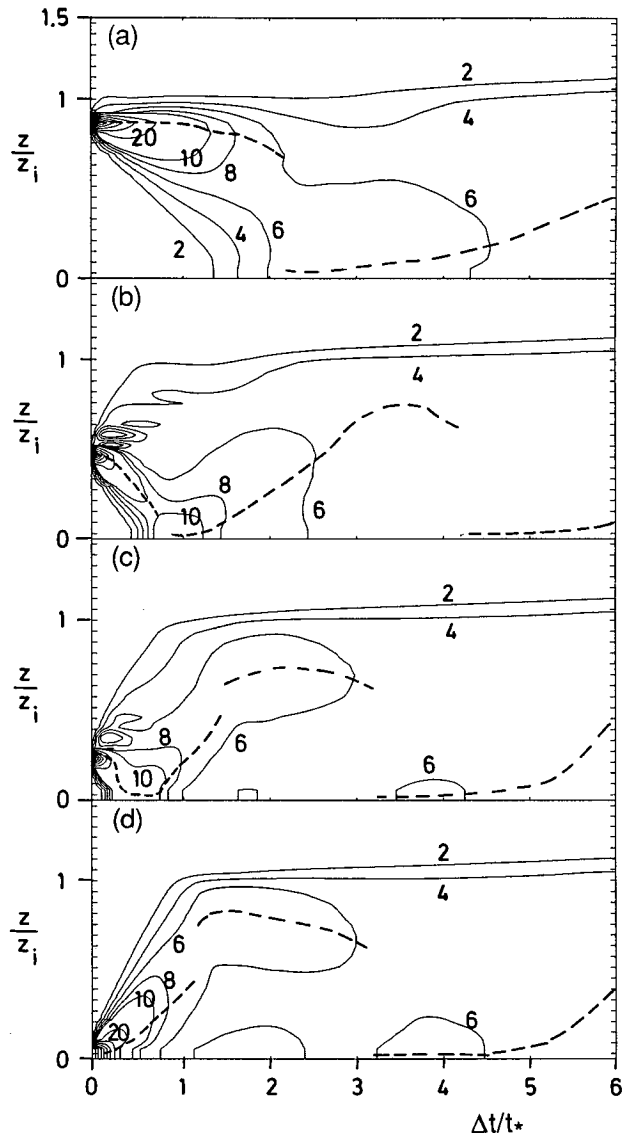

FIG. 6. Transport diagram showing isolines of $c_{ij}(\Delta t)$ as a function of $\Delta t/t_*$ for selected source levels, j, corresponding to levels $z/z_i =$: (a) 0.91, (b) 0.47, (c) 0.22, and (d) 0.03. Contour levels are in percent of the original concentration. The heavy dashed line indicates the concentration maximum.

version sinks below the middle of the mixed layer before rising back to $0.5z_i$. The behavior of $\bar{z}_j$ with time agrees well with the dispersion from point sources in the laboratory tank measurements of Willis and Deardorff (1976, 1978, 1981). The simulated mean upward transport from $z/z_i \approx 0.2$ was slightly greater than the observations, and the mixing of surface air occurs a bit more slowly in the simulation than in the observations. After four time units all of the tracers originating below the inversion have been mixed evenly. Tracers from just above the inversion are entrained down into the CBL.
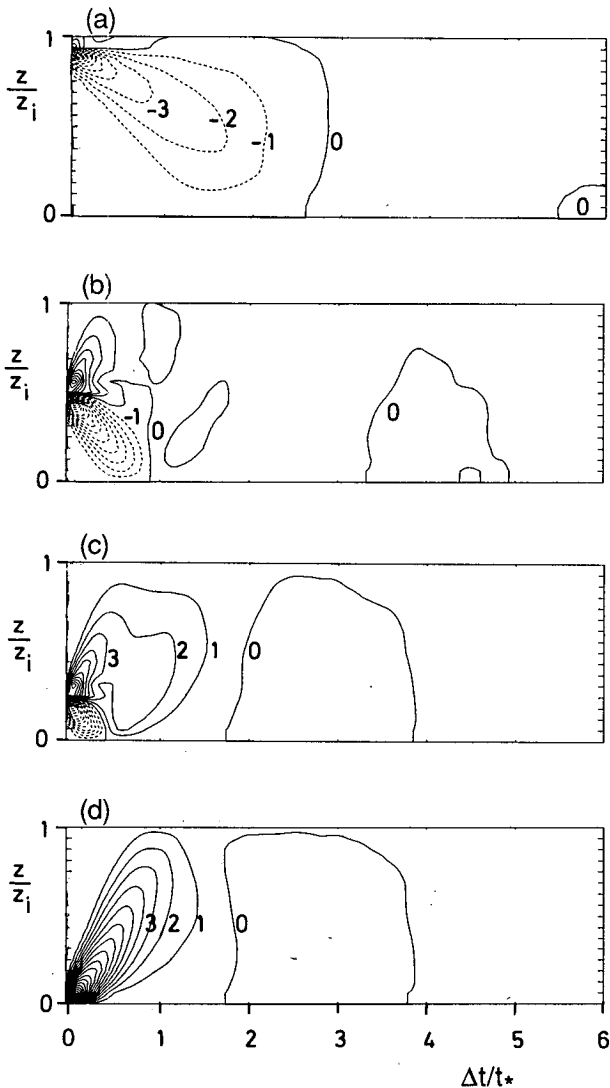
FIG. 7. Vertical flux of tracers as a function of $\Delta t / t_*$, for the same source levels as in Fig. 6. Contour levels are in percent of w_* (assuming unit initial concentration).

A measure of the spread of the concentration distribution is the vertical dispersion parameter, $\sigma_j(\Delta t)$, defined by

$$\sigma_j^2(\Delta t) = (\Delta z)^2 \sum_{i=1}^{n} c_{ij}(\Delta t) \cdot (i - j)^2 \qquad (10)$$

(Stull 1986). This quantity reflects the amount of vertical mixing which has taken place. Figure 9 shows the dispersion for several layers in the model. Tracers from the middle of the CBL are mixed the most rapidly, with the dispersion reaching an equilibrium value of approximately 0.3 after about one-half time unit. Tracers from the bottom and top of the mixed layer are slower to disperse because the flow is limited by the surface and the capping stable layer. The dispersion
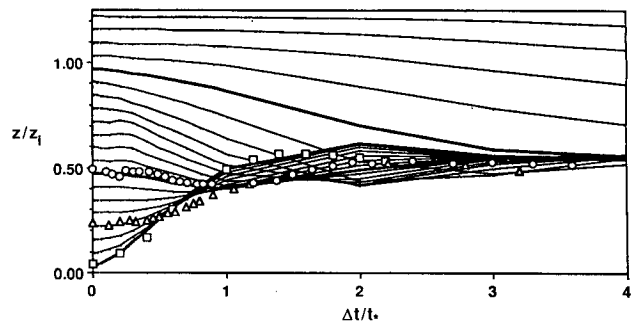
FIG. 8. Mean height, $\bar{z}_j(\Delta t)$, of tracers originating at each level, j, as a function of time. The experimental results of Willis and Deardorff (1976, 1978, 1981) are also plotted, corresponding to the heights of $z/z_i = 0.04$ ($\square$), 0.24 ($\triangle$), and 0.49 ($\bigcirc$).

for surface tracers equilibrates after approximately three time units. The dispersion of tracers at the highest stable level in the model is much smaller than that for mixed layer air at all timesteps, and describes the dispersion caused by numerical noise. Again, the dispersion calculated from the transilient coefficients agrees quite well with the laboratory results of Willis and Deardorff (1976, 1978, 1981), except for the case of $z/z_i \approx 0.2$, where the calculated dispersion is about 20% greater than the observed. At $z/z_i = 0.34$ our vertical dispersion is also larger than that measured during the CONDORS experiment (Eberhard et al. 1988) by about 20%. These differences are to be expected because in the field experiments the tracers diffuse both vertically and laterally, while in this simulation the lateral dispersion is irrelevant because of the layered source distribution.

d. Asymmetry of vertical mixing process velocity

Transilient matrix asymmetry is related to the skewed probability distribution of vertical velocity that is typically found in a convective mixed layer. Each element along the main diagonal (thick shaded line in Fig. 10a) of the matrix corresponds to one individual grid layer (index $= r$), and serves as a reference height, as illustrated with the dotted lines. Through any reference height, we can draw a cross-diagonal line,
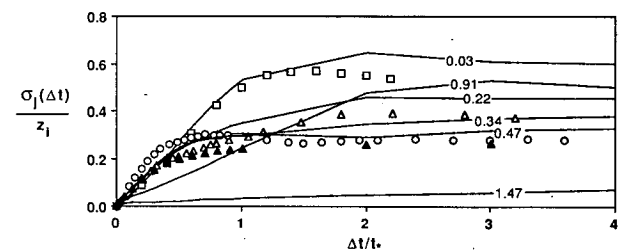

FIG. 9. As in Fig. 8, for the dispersion, $\sigma_j(\Delta t)$, at selected vertical levels. The atmospheric measurements of Eberhard et al. (1988) ($\blacktriangle$) are included, corresponding to a release height of $z/z_i = 0.32$.
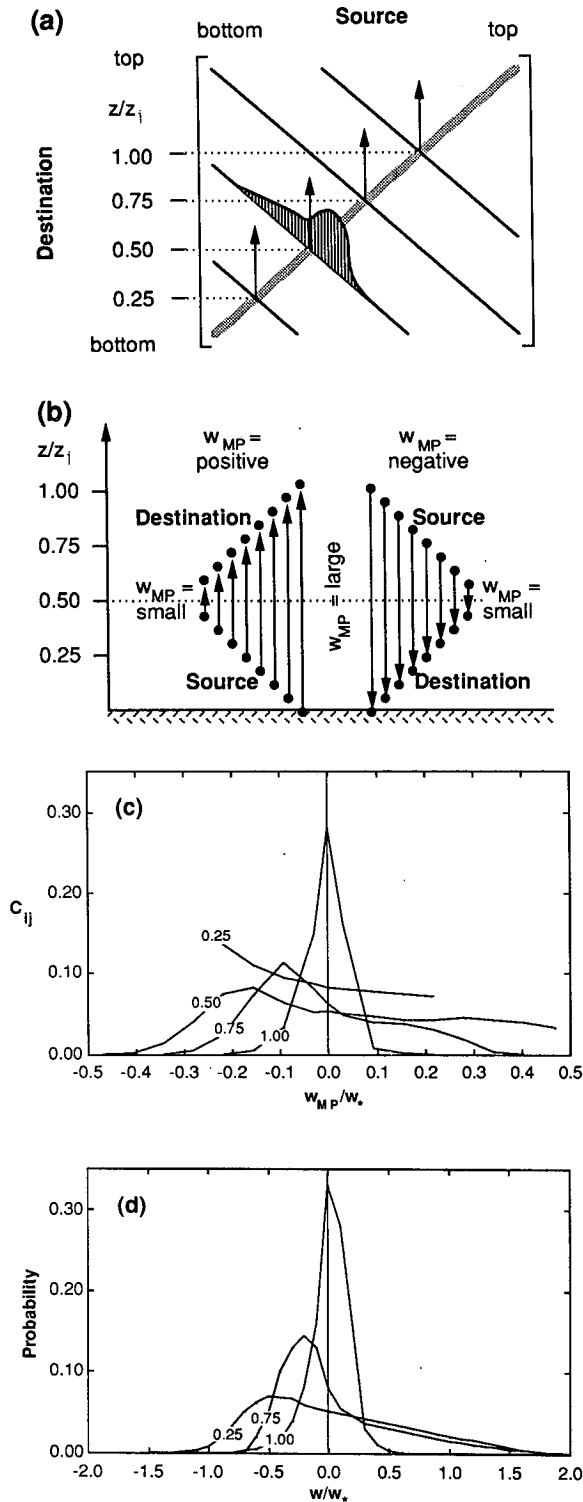
sketched as the solid line. Matrix elements along this cross-diagonal have the special characteristic that their source and destination locations are equidistant from the reference height, with one location above the reference and the other below (Fig. 10b).

A matrix element on this cross-diagonal that is two elements away from the main diagonal, for example, describes the fraction of air that started from two grid points below (above) the reference level, and ended two grid points above (below). This corresponds to transport across a net distance of $4\Delta z$ during the time interval Δt for which the matrix was evaluated. A net mixing-process velocity, w_{MP}, associated with this transport is easily defined by $w_{MP} = (i - j)\Delta z/\Delta t$, where i and j are the destination and source indices, respectively. Here we are focusing on only a special relationship between i and j, that is, $i - r = r - j$.

The largest-size eddy considered is that which hits a model boundary such as the ground, and the smallest size is $2\Delta z$. Between these limits is a range of eddy sizes, subject to the constraint that the destination and source locations of the parcel be equidistant from the reference height. Such net transport velocities across finite distances, w_{MP}, inherently differ from the local w-velocity measured at one height.

The fractions of air (i.e., c_{ij}) associated with various mixing process velocities for $\Delta t/t_* = 1.0$ are shown in Fig. 10c, and are compared to the corresponding probability distributions of state w found by Schmidt (1988) during previous simulations with the same LES model (Fig. 10d). The transilient results show a positively skewed distribution of w_{MP} throughout most of the mixed layer, changing to a narrower and slightly negatively skewed distribution at the top of the mixed layer. These shapes not only agree with Schmidt's results for state w (except at $z/z_i = 0.25$), but also agree with other distributions in the published literature (Stull 1988c).

The magnitudes of vertical velocity, however, are quite different, as is to be expected. The instantaneous w values of Fig. 10d are about a factor of 3 larger than the w_{MP} velocities of Fig. 10c. An air parcel with large state w might move rapidly upward, and then rapidly downward again during a time interval Δt. The net difference in starting and ending locations of the parcel might be small, corresponding to a small w_{MP}. Since Fig. 10c corresponds to net transport during one convective timescale ($\Delta t = t_* = 18.3$ min), we would anticipate that many of the air parcels have had time to change their vertical direction of motion as they follow the normal closed circulations expected in a convective mixed layer.

FIG. 10. (a) Schematic diagram showing a cross-diagonal distribution of transilient matrix elements at a reference height of $z/z_i = 0.5$. (b) Net mixing-process velocities, defined by $w_{MP} = (i - j)\Delta z/\Delta t$, are shown as vectors for the special cross-diagonal set of source (j) and destination (i) locations. (c) Distribution of the fraction of air (c_{ij}) associated with mixing process velocities at several heights as a function of w_{MP}, based on the LES forecast of tracer movement during $\Delta t/t_* = 1.0$. (d) Probability distribution of instantaneous values of state vertical velocity, w, averaged over horizontal grid layers in the LES model at a time when it was in near steady state. Note the differing scales on diagrams (c) and (d).

e. Asymmetry of transport

The transilient matrices in Fig. 5 clearly show that the mixing of air from a given level is generally not symmetric in the upward and downward directions. It follows that the transport of air from a level should differ from the transport of air toward that level.

First we compare the fractional amounts of concentration transported upward as opposed to downward *from* a given level. These are computed from the *columns* of the transilient matrix by summing over all destinations, i, above or below the source, respectively:

$$f_j^\uparrow(\Delta t) = \sum_{i=j+1}^{n} c_{ij}(\Delta t), \quad f_j^\downarrow(\Delta t) = \sum_{i=1}^{j-1} c_{ij}(\Delta t). \quad (11a,b)$$

The fraction remaining at the jth level is c_{jj}.

Early in the simulation, before the convective mixing has proceeded very far, the little amount of fluid transport that occurs is similar in the upward and downward directions at all levels away from the surface, as seen in Fig. 11a. For $\Delta t/t_* = 0.2$ the maximum upward transport occurs for surface air, while the maximum downward transport is found at midlevels in the CBL (Fig. 11b). The solid line shows that mixing rapidly moves air away from its original grid level. Initially the strongest removal occurs near the surface, but the minimum in c_{jj} gradually moves toward the middle of the CBL. Most of the transport of CBL air is downward for $\Delta t/t_* \leqslant 1.0$ (Fig. 11b, c, d). This is in agreement with the conditional sampling results of Greenhut and Khalsa (1987) and Young (1988), who examined the fractional areas of upward and downward vertical velocity in the CBL.

With time the peak in the downward transport rises until it reaches the inversion level. At the same time the surface air continues to be mixed upward most rapidly, while a minimum in upward transport occurs just beneath the cappping inversion (except for air
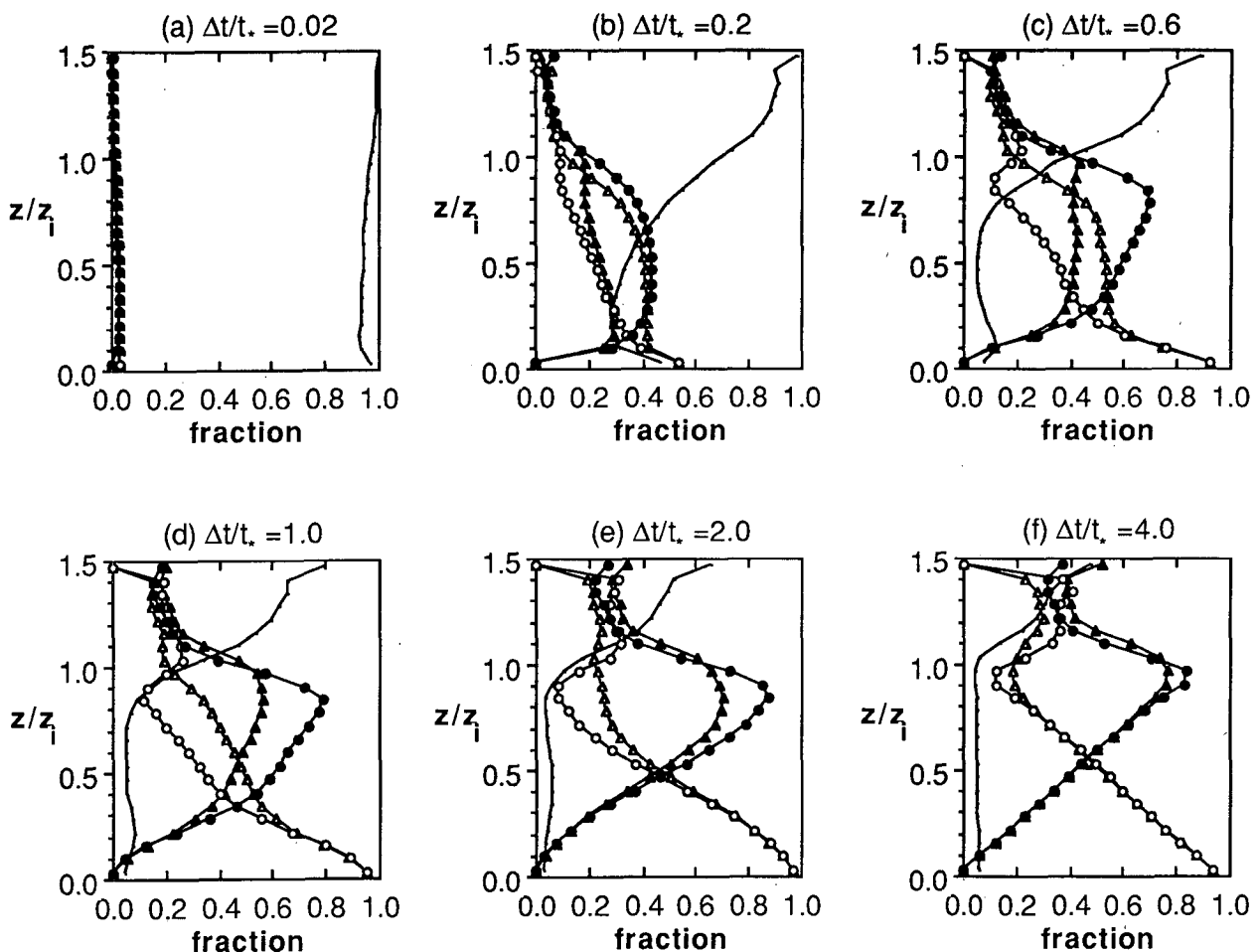

FIG. 11. Fraction of air transported upward and downward at each level for selected time intervals, $\Delta t/t_* =$: (a) 0.02, (b) 0.2, (c) 0.6, (d) 1.0, (e) 2.0, (f) 4.0. The transport upward and downward from each *source* level is given by $f_j^\uparrow(\Delta t)$, (O), and $f_j^\downarrow(\Delta t)$, (●), respectively, and the transport upward and downward toward each *destination* level is given by $f_i^\uparrow(\Delta t)$, (▲), and $f_i^\downarrow(\Delta t)$, (△), respectively. The solid line indicates the fraction of air not subjected to resolvable transport.

originating at the uppermost level where the model constrains the upward transport to be zero). The level at which $f_j^\uparrow = f_j^\downarrow$ is low in the CBL for short time intervals, then shifts upward for longer values of $\Delta t / t_*$. After several time units the unmixed fraction $c_{jj} = (24/1.5)^{-1} \sim 0.06$, and the upward and downward fractional transports achieve an approximately linear profile in the boundary layer, given by $f_j^\uparrow \approx 0.94 - f_j^\downarrow$ and $f_j^\downarrow \approx 0.94\, z/z_i$ (Fig. 11f). The upward and downward transports are of equal magnitude at $z/z_i \sim 0.5$. This is what we theoretically expect for complete mixing of CBL air.

The partial sums of the transilient coefficients along a *row* in the matrix give the fractions of air which were transported upward or downward *toward* a given destination level:

$$f_i^\uparrow(\Delta t) = \sum_{j=1}^{i-1} c_{ij}(\Delta t), \quad f_i^\downarrow(\Delta t) = \sum_{j=i+1}^{n} c_{ij}(\Delta t). \quad (11c,d)$$

Profiles of $f_i^\uparrow$ and $f_i^\downarrow$ are also shown in Fig. 11. As in the previous case for transport away from a level, the upward and downward components are equal only for very short time intervals. For $\Delta t / t_* \leqslant 1.0$, most levels in the CBL contain a greater fraction of air transported downward from above than upward from below. Only near the inversion has the original air been replaced by air originating at lower levels (Fig. 11b, c, and d). With increasing time the level at which $f_i^\uparrow = f_i^\downarrow$ moves downward from the inversion level to 0.5 z/z_i, and the profiles approach the linear profiles expected for the well mixed CBL.

Comparing the transport *toward* a level with the transport *from* a level, one sees that except at the earliest and latest time points, large differences exist between the shapes of the curves. The fractional transport away from a level approaches equilibrium much faster than the fractional transport toward that level, as expected because $c_{ij} \neq c_{ji}$. For symmetric mixing, i.e., for a symmetric transilient matrix, it is easy to show that $f_i^\uparrow = f_j^\downarrow$ and $f_j^\uparrow = f_i^\downarrow$. The differences between the curves in Fig. 11 are another measure of the asymmetry of the mixing produced by the LES model for intermediate time intervals.

f. Mixing lengths

The concept of a mixing length can be used to describe the average distance a parcel moves during the mixing process. The mixing length depends on the relative amount of air transported across various vertical distances and is, therefore, a function of height. Based on the discussion in the previous section, we should also expect the mixing length to depend on the direction of the mixing. We use the column values of c_{ij} to estimate upward and downward mixing lengths, $l_j^\uparrow$ and $l_j^\downarrow$, as weighted average displacements *from* the source level j,

$$l_j^\uparrow(\Delta t) = \frac{\Delta z \sum\limits_{i=j}^{n} c_{ij}(\Delta t) \cdot |i - j|}{\sum\limits_{i=j}^{n} c_{ij}(\Delta t)},$$

$$l_j^\downarrow(\Delta t) = \frac{\Delta z \sum\limits_{i=1}^{j} c_{ij}(\Delta t) \cdot |i - j|}{\sum\limits_{i=1}^{j} c_{ij}(\Delta t)}. \quad (12a,b)$$

Similarly we can compute the mixing lengths for upward and downward transport *to* a given destination level i,

$$l_i^\uparrow(\Delta t) = \frac{\Delta z \sum\limits_{j=1}^{i} c_{ij}(\Delta t) \cdot |i - j|}{\sum\limits_{j=1}^{i} c_{ij}(\Delta t)},$$

$$l_i^\downarrow(\Delta t) = \frac{\Delta z \sum\limits_{j=i}^{n} c_{ij}(\Delta t) \cdot |i - j|}{\sum\limits_{j=i}^{n} c_{ij}(\Delta t)}. \quad (12c,d)$$

Initially the values of $l_j^\uparrow$ and $l_j^\downarrow$ are small and nearly symmetric about the level of origin (Fig. 12a). At $\Delta t / t_* = 0.2$ (Fig. 12b) the mixing lengths for upward transport from a given level exceed those for downward transport throughout most of the boundary layer, while the fraction of air transported downward is greater than the fraction transported upward (Fig. 11b). This supports the qualitative picture of narrow buoyant updrafts separated by broader regions of slower, downward moving air. At intermediate time intervals $l_i^\uparrow$ is greater than $l_j^\downarrow$ in the upper part of the CBL, and $l_i^\downarrow$ is less than $l_j^\uparrow$ in the lower part of the CBL. As the mixing proceeds the mixing lengths approach a linear dependence on height (Fig. 12d, e, f), with $l_i^\uparrow$ and $l_j^\uparrow$ approaching linearity more rapidly than $l_i^\downarrow$ and $l_j^\downarrow$. This reflects the greater speed of the updrafts over that of the downdrafts. The largest mixing lengths correspond to upward transport of surface air and downward transport of inversion-level air. The upward and downward mixing lengths are equal only at $z/z_i \sim 0.5$, with increasing asymmetry away from that level.

An equation for overall mixing length, l_k, at level k is simply

$$l_k(\Delta t) = \Delta z \sum_{i=1}^{n} \frac{1}{2} [c_{ik}(\Delta t) + c_{ki}(\Delta t)] \cdot |i - k|. \quad (13)$$

This equation represents a weighted sum of the upward and downward transport both toward and from the level k. Figure 13 shows that with increasing time the overall mixing length increases in magnitude, with the level of the maximum value splitting from the lower CBL at small $\Delta t / t_*$ to the surface and inversion level. This splitting is evident as early as $\Delta t / t_* = 0.6$, when
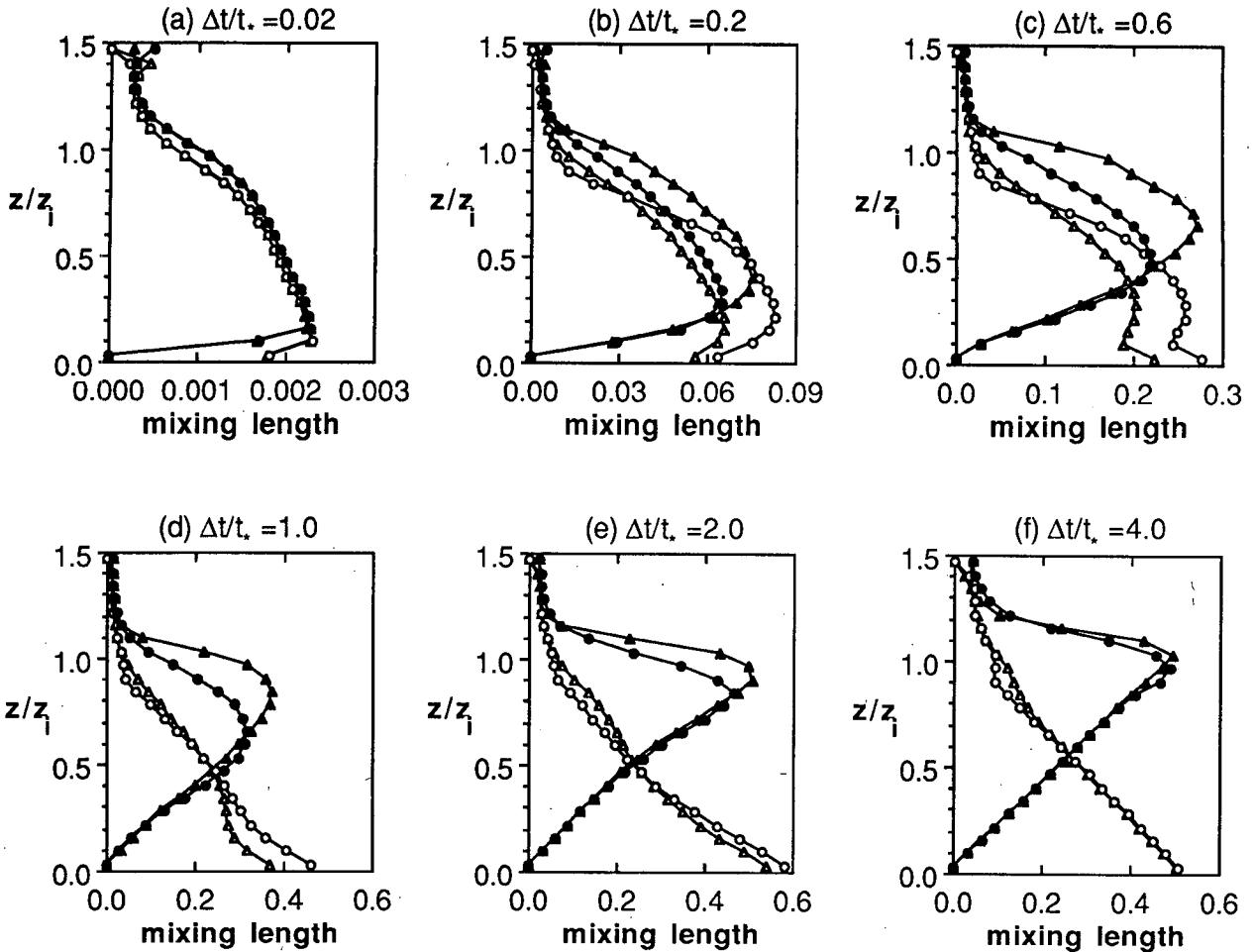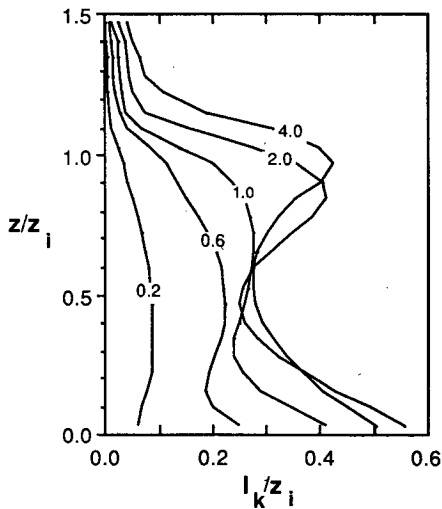
FIG. 12. Normalized mixing length for air transported upward and downward at each level for selected time intervals, $\Delta t / t_* =$: (a) 0.02, (b) 0.2, (c) 0.6, (d) 1.0, (e) 2.0, (f) 4.0. The normalized mixing length upward and downward from each *source* level is given by $l_j^\dagger (\Delta t) / z_i$, (O), and $l_j^\downarrow (\Delta t) / z_i$, (●), respectively, and the normalized mixing length for air transported upward and downward toward each *destination* level is given by $l_i^\dagger (\Delta t) / z_i$, (▲), and $l_i^\downarrow (\Delta t) / z_i$, (△), respectively.

FIG. 13. Normalized mixing length, $l_k (\Delta t) / z_i$, for selected time intervals.

air from near the surface is transported rapidly upward in updrafts, producing large mixing lengths at the lowest level. At large $\Delta t / t_*$ air near the boundaries of the mixed layer can travel farther on average than air from the midlevels, which feels the confining effects of both vertical boundaries.

g. Process spectra

The process spectrum, introduced by Stull (1988c, d), spectrally decomposes the total mixing at a level into contributions of different-size mixing processes originating from different locations. It is analogous to the transport spectrum discussed in section 2, except that it measures the relative magnitudes of the mixing processes themselves, regardless of the fluxes associated with them. The process spectrum, $P_{k|m}$, is the contribution to the mixing from each eddy size, $m\Delta z$ (which we also loosely refer to as the "wavelength") at the height $k\Delta z$, and follows from Fig. 3 and Eq. (4):
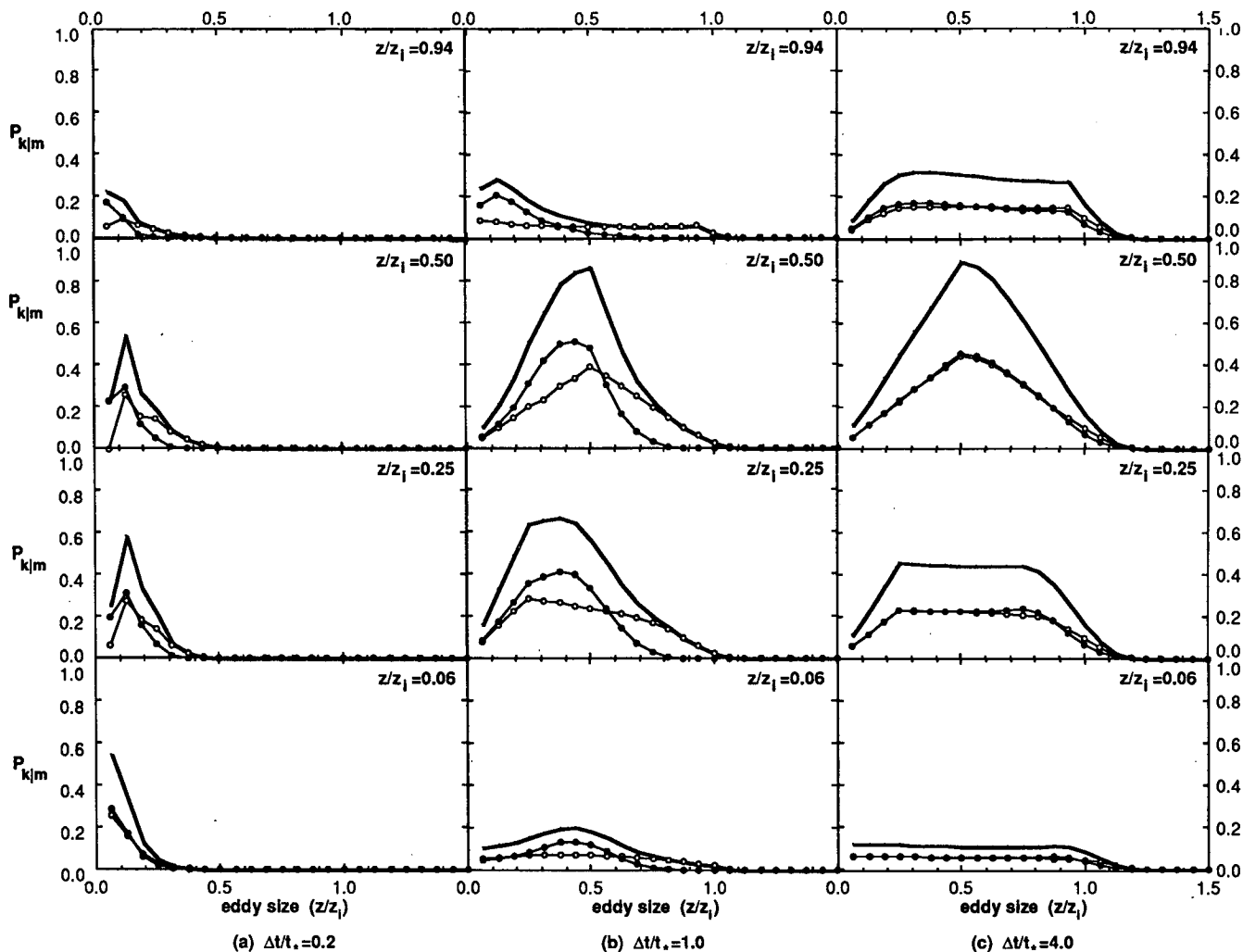
FIG. 14. Process spectra, $P_{k|m}(\Delta t)$, for selected heights and time intervals, $\Delta t/t_* =$: (a) 0.2, (b) 1.0, (c) 4.0. The total process spectrum is given by the heavy solid line, the upward component by the open circles (O), and the downward component by the closed circles (●).

$$P_{k|m}(\Delta t) = \sum_{i=1}^{k} \sum_{j=k+1}^{n} \delta_{m,|i-j|}[c_{ij}(\Delta t) + c_{ji}(\Delta t)]. \quad (14)$$

The magnitude of $P_{k|m}$ reflects the "vigor" of the mixing. The portion of $P_{k|m}$ which includes c_{ij} represents the contribution from downward mixing processes, and the portion including c_{ji} is the contribution from upward mixing processes (refer to Fig. 3).[1]

----

[1] Note that the original equation for process spectra suggested by Stull (1988c,d) is incorrect. First, it applies only to symmetric matrices. Second, it is too small by a factor of two. Third, it includes the effects of eddies that do not cross the level of interest, k. Due to a fortuitous trick in computer programming, however, the graphs of process spectra presented by Stull (1988c,d) are correct, except that the magnitudes of the spectra are too small by a factor of two. The process spectra shapes of Stull (1988c,d) are still valid, as are the associated physical interpretation. We recommend that (14) be used for all process spectra calculations, because it is valid for both symmetric and asymmetric transilient matrices.

Figure 14 gives the process spectra for selected altitudes and time intervals. For very short time intervals, $P_{k|m}$ is small at all wavelengths because most of the air still remains in its original grid box (refer to Fig. 11a). For longer time intervals the mixing processes mix greater amounts of air across longer distances. Thus both the magnitude of $P_{k|m}$ and the wavelength, $m\Delta z$, corresponding to the dominant eddy size tend to increase with Δt. Near the surface ($z/z_i = 0.06$) vigorous mixing takes place for short time intervals (Fig. 14a), then decreases with time as a broader range of eddy sizes influences the mixing (Fig. 14b, c). The spectral broadening for upward eddies is more rapid than that for downward eddies, although both lead to a shift toward larger wavelengths. Deeper inside the CBL ($z/z_i = 0.25$, $z/z_i = 0.50$) the mixing quickly becomes more vigorous than at the surface, and larger wavelengths become relatively more important. By $\Delta t/t_* = 1.0$ the peak wavelengths are on the order of $0.5z_i$ inside the

CBL (Fig. 14b). Again, because of the greater speed of the updrafts, the upward component of $P_{k|m}$ dominates the spectrum of the larger eddy sizes. Near the inversion the process spectra remain small, limited to wavelengths of $1\Delta z$–$2\Delta z$ for most time intervals. The capping stable layer inhibits upward motion at $z/z_i = 0.94$, and the slower downward transport of inversion level air is not as effective as the upward transport of surface air in thermals.

The symmetric structure in Fig. 14c represents the equilibrium (with respect to timestep) process spectra for a well mixed CBL. At each level there exists a range of intermediate distances across which the mixing is approximately equal. We emphasize that $P_{k|m}$ represents the net effect of many sizes of physical eddies in transporting air across a distance $m\Delta z$. After several time units the values of the transilient coefficients are nearly the same everywhere in the CBL. If we treat the mixing coefficients as constant, i.e., $c_{ij}(\Delta t \to \infty) = c$, then it is easy to show that

$$P_{k|m} = \begin{cases} 2c \cdot \min(m, k), & k \leq \frac{1}{2} n_i \\[2ex] 2c \cdot \min(n_i - m, n_i - k), & k > \frac{1}{2} n_i \end{cases} \quad (15)$$

where n_i is the index of the uppermost CBL grid box. The flat portions of the curve represent scales of mixing which are inhibited by the presence of either the surface or the capping stable layer. The curve slopes toward zero on both sides of the diagram because there are fewer terms in the summation [i.e., fewer (i, j) for which exchanges of length $m\Delta z$ can occur].

The area under the spectrum is related to the total mass of air transported upward and downward past each level, which can be interpreted as a measure of mixing intensity, P_k. We sum $P_{k|m}$ across all wavelengths, m, which is the same as removing the Dirac delta function in (14), to obtain

$$P_k(\Delta t) = \sum_{i=1}^{k} \sum_{j=k+1}^{n} [c_{ij}(\Delta t) + c_{ji}(\Delta t)]. \quad (16)$$

Figure 15 shows the mixing intensity as a function of height and time interval. The P_k is small at all levels for small Δt, then grows with time as the mixing develops. The maximum mixing intensity moves upward from the lower CBL to the mid-CBL, and P_k approaches an asymptotic profile defined by

$$P_k(\Delta t \to \infty) = \frac{2k}{n_i} (n_i - k) \quad (17)$$

for the well mixed CBL. Equation (17) follows directly from (16) in the special case of constant c_{ij} everywhere in the mixed layer. The departure of the profile at $\Delta t / t_* = 4.0$, which is essentially well mixed, from the asymptotic profile, is again due to numerical diffusion.

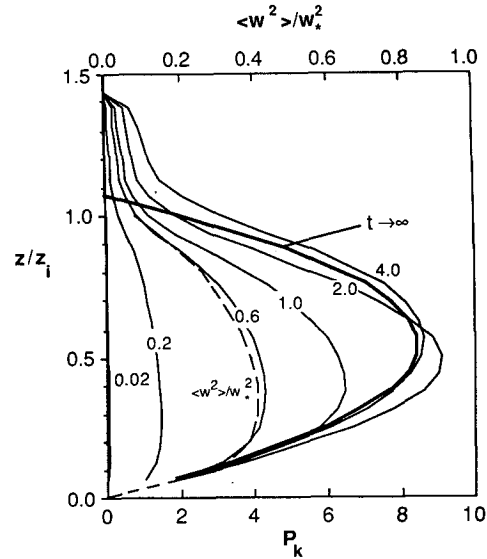The shape of the mixing intensity curves is strikingly

FIG. 15. Mixing intensity, $P_k = \sum_{m=1}^{n-1} P_{k|m}$, as a function of dimensionless height, z/z_i, for selected time intervals. The vertical velocity variance profile, normalized by w_*^2, is plotted as the dashed line (Schmidt and Schumann 1989).

similar to the shape of the vertical velocity variance, $\langle w^2 \rangle$, also plotted in Fig. 15. This $\langle w^2 \rangle$, which was previously computed by Schmidt and Schumann (1989) using the same LES model, initial and boundary conditions, is a "state" statistic based on instantaneous measures of w. Thus, it is expected to correspond more closely to the shorter time-interval mixing intensities.

h. Air transport spectra

In section 2 expressions were given for the total flux and transport spectrum of a passive scalar [Eqs. (3) and (4)]. The total mass flux of air through each level must equal zero because of mass continuity, but the contributions from different sizes of mixing processes may be nonzero. Since at the initial time $\Psi_j = 1$ at each level j, Eq. (4) can be simplified to give the transport spectrum for air (mass) flux,

$$F_{k|m}^{\text{air}}(\Delta t) = \frac{\Delta z}{\Delta t} \sum_{i=1}^{k} \sum_{j=k+1}^{n} \delta_{m,|i-j|} [c_{ji}(\Delta t) - c_{ij}(\Delta t)]. \quad (18)$$

This expression is nearly the same as (14) for the process spectrum, except that the difference of the upward and downward components, rather than the sum, determines the net air flux through level k due to mixing processes across a vertical distance of $m\Delta z$.

Figure 16 shows the air transport spectra for selected levels and time intervals. The phrase "vertical transport distance" is used here instead of "eddy size" because this spectrum is more easily interpreted as air parcel
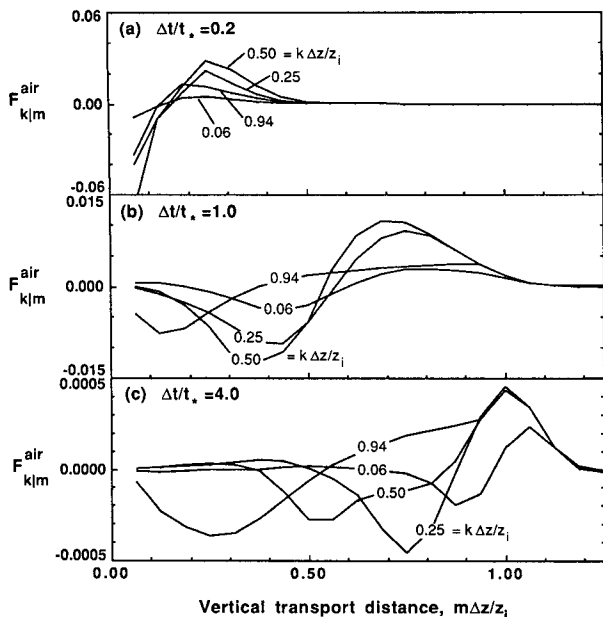
FIG. 16. Transport spectrum, $F^{air}_{k|m}(\Delta t)$, for vertical air mass flux at selected heights, $k\Delta z/z_i$, and time intervals, $\Delta t/t_* =$: (a) 0.2, (b) 1.0, (c) 4.0. Note the change of vertical scale.

movements. Instead of continuing to grow with time, as did the process spectrum, $F^{air}_{k|m}$ has its largest values after relatively short time intervals when the mass flux is concentrated in relatively small parcel displacements. With increasing $\Delta t/t_*$, $F^{air}_{k|m}$ decreases as the mass flux is spread over a greater range of parcel displacements. Downward net transport takes place across smaller distances, while an equivalent amount of net upward transport is accomplished across larger distances. It is interesting that for $\Delta t/t_* \leqslant 1.0$, values of $F^{air}_{k|m}$ for heights $z/z_i = 0.06, 0.25$, and 0.50 cross the origin at approximately the same vertical transport distance (Fig. 16a, b). This suggests that even though the process spectra showed significantly different eddy size distributions with height (see especially Fig. 14b), the net transport across these various distances behaves similarly near the surface and in the middle of the CBL. Only the magnitude of $F^{air}_{k|m}$ is dependent on height for $\Delta t/t_* \leqslant 1.0$. Just below the inversion a net downward mass flux across small distances is balanced by a small net upward transport accomplished over a wide range of distances. After 4 time units the mass transport spectrum for air is very small. What little net transport remains is controlled by the larger parcel displacements, and probably also by the entrainment causing slow growth of the CBL height, z_i.

5. Equivalent-timestep matrix comparisons

A transilient matrix is, by necessity, a function of both the physics, the time, and the timestep increment. For stationary turbulence, as is approximated by the LES, the transilient matrices are not a function of time

but continue to be a function of timestep. In this section we attempt to remove the influence of the timestep from our matrix comparison.

Because successive matrix multiplications are used to generate a forecast, we can use a matrix valid for a short timestep, Δt_1, to calculate the corresponding matrix that would cause the same amount of mixing over a larger timestep, $\Delta t_2 = p\Delta t$:

$$
\begin{aligned}
\langle \Psi(t + p\Delta t_1) \rangle \\
&= [c(\Delta t_1)] \cdot [c(\Delta t_1)] \cdots [c(\Delta t_1)] \cdot \langle \Psi(t) \rangle \\
&= [c(\Delta t_1)]^p \cdot \langle \Psi(t) \rangle \\
&= [c(\Delta t_2)] \cdot \langle \Psi(t) \rangle.
\end{aligned}
$$

The matrix $[c(\Delta t_2)]$, it is hoped, describes the same physics as $[c(\Delta t_1)]$, but over a longer timestep. We can thus convert the raw matrices of section 4a to correspond to some larger reference timestep, Δt_2, using

$$
[c(\Delta t_2)] = [c(\Delta t_1)]^{\Delta t_2/\Delta t_1}. \tag{19}
$$

In addition to taking the power of a matrix to change its timestep as is done here, one can take roots of a matrix by finding the eigenvectors and eigenvalues, taking the roots of the eigenvalues, then multiplying again by the eigenvectors to obtain a new matrix.

We use a reference timestep of $\Delta t = 2t_* = 36.53$ min, and take the matrices of smaller timesteps to the appropriate power to bring them up to this reference. The matrix powers were done in double precision (64 bits) to ensure that small elements away from the main diagonal would have the proper influence.

Since the fluid dynamics is quasi-stationary, one would anticipate that all of the matrices should look similar when applied over a common timestep. The results shown in Fig. 17, however, reveal that the matrices are very dissimilar. We will use Fig. 5e as the reference, and refer to the detailed description of this matrix given in section 4a.

The matrix of $[c(1t_*)]^2$, contoured in Fig. 17a, indicates that the CBL is fairly well mixed but the mixing processes are not symmetric. Inversion level air is still transported efficiently to the surface, even though the upward mixing process velocities are greater than the downward w_{MP}'s. The free atmospheric diffusion is still fairly small. However, there appears to be less convective overturning, but more uniform mixing within the mixed layer. This is somewhat surprising, because Fig. 5e indicates overturning (relatively large values along a cross diagonal through the mixed layer). Also, there is no longer a relative minimum at the lower left corner, which is also associated with the more uniform mixing.

In Fig. 17b, for matrix $[c(0.5t_*)]^4$, we see even more dramatic changes. The matrix is becoming more symmetric, a larger amount of air is not mixed out of the surface layer, there is no evidence of convective overturning, and the mixed layer is less well mixed. The upward w_{MP} is still slightly greater than for downward
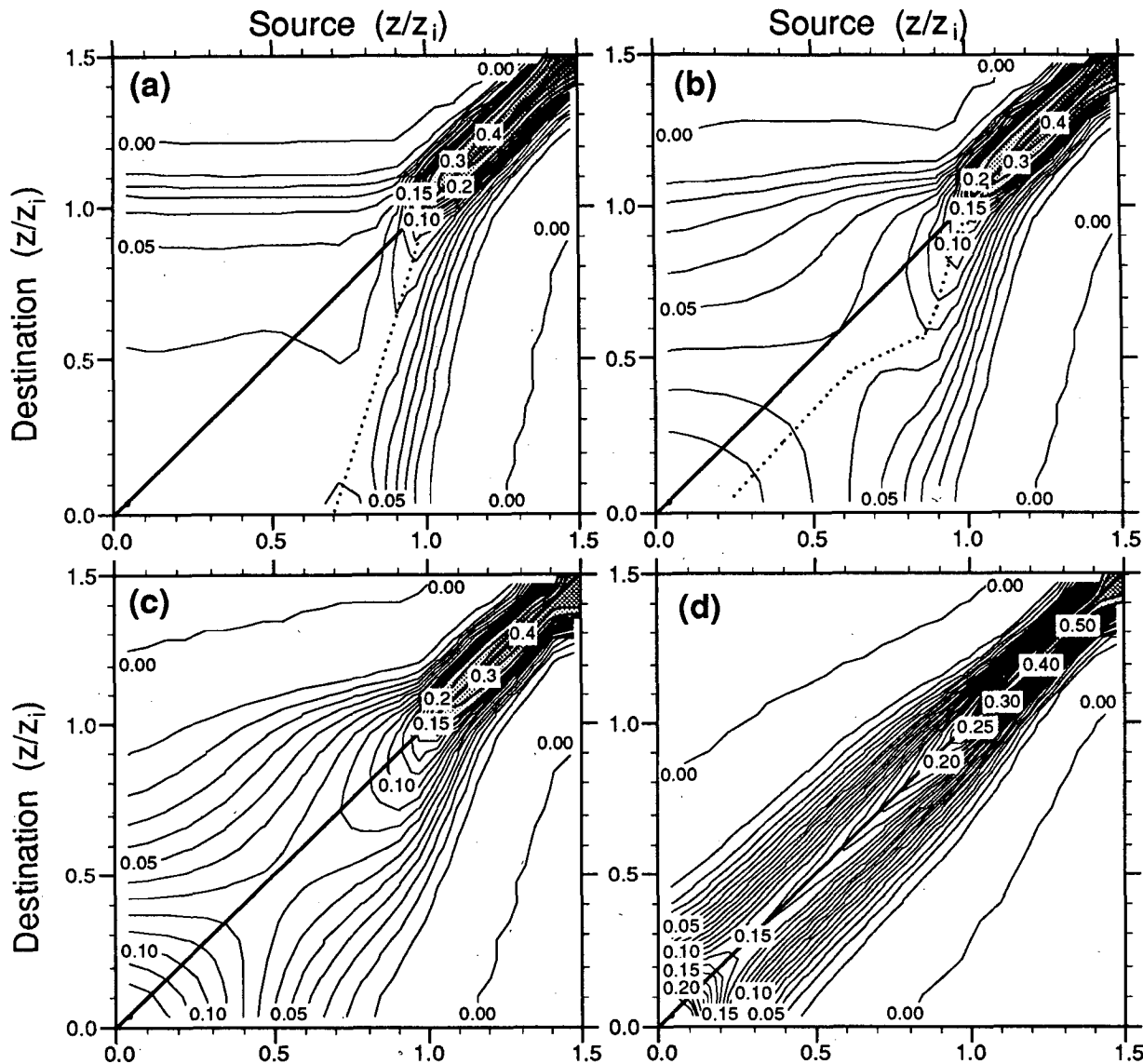
FIG. 17. Contours of transilient turbulence matrices after the matrices were taken to the appropriate powers to bring them to an effective final timestep of $\Delta t_2 = 2t_* = 36.53$ min. The original timesteps $\Delta t_1/t_*$ were: (a) 1.0, (b) 0.5, (c) 0.2, and (d) 0.02. The corresponding exponents of the powers are: (a) 2, (b) 4, (c) 10, and (d) 100.

mixing, but this is partly due to numerical diffusion problems rather than physics.

Figure 17c, for matrix $[c(0.2t_*)]^{10}$, shows that almost all of the apparent physical characteristics are different from those of Fig. 5e, except for the numerical diffusion in the free atmosphere. There is still more mixing in the mixed layer than above, but the mixing is much more symmetric, and is taking on the characteristics of small-eddy-diffusivity (K) theory. Figure 17d, for matrix $[c(0.02t_*)]^{100}$, shows a continuation of this trend. Indeed, in Fig. 17d, the physical mixing within the mixed layer is more difficult to distinguish from the numerical noise within the free atmosphere.

The differences between Figs. 5e and 17a–d are dif-

ficult to explain at first, because they are based on the measurement of the same tracers within the same steady-state LES convective mixed layer with effectively identical timesteps. However, we see two reasons for these differences. The first originates from the time dependence of *flux dynamics* even for a homogeneous turbulent velocity field. The second is related to the vertical extent and *convective structure* of the CBL. To explain the first reason, we recall the prognostic equation for the vertical turbulent flux of any tracer (e.g., Stull 1988c) in the CBL,

$$\frac{\partial}{\partial t} \langle w\Psi \rangle = - \langle w^2 \rangle \frac{\partial \langle \Psi \rangle}{\partial z} + \beta g \langle \Psi T \rangle - \nu$$

where ν comprises diffusion, dissipation and pressure effects on $\langle w\Psi \rangle$. This equation shows that time (of order t_*) is required to adapt the fluxes to gradient and buoyancy forcings. The fluxes are zero initially because the tracer fluctuations are zero. They become nonzero very quickly because of large vertical velocity fluctuations and the initially very steep concentration gradients. Later in the simulation, as the tracer concentration gradients weaken, their influence on the flux tendency becomes less important. The fluxes are responsible for changes in the mean concentration profiles within a time interval and it is these profiles which form the columns of the transilient matrix. Hence, the evolution of the flux dynamics causes the early and late evolution of the transilient matrix to possess different characteristics.

The second reason for the observed differences is the convective structure memory, or lack thereof, of the transilient matrices. Initially after tracer injection, some of the tracer mass is carried upward in the thermals, and some is carried downward. During a short time interval, the tracers from low altitude sources that happen to be within thermals are carried upward a short distance, where they contribute to the total concentration at that destination height. The transilient matrix for this short timestep captures the net mixing between that source and destination, but does not contain information that the tracers are still within the thermals. During the next short time interval, the tracers in the real CBL are carried further upward within the same thermals, leading to transport across larger distances during the extended time period. However, because the small-timestep transilient matrix has lost the information that all of the tracers are still in the thermals, it transports only a small fraction of the tracers further upward. Thus, the net transport generated by the repeated application of a small-timestep matrix is smaller and more local than the single application of a large-timestep matrix.

At first glance, this concept appears to be the same as *relative* puff dispersion (Sawford 1988), where different physics is happening on different scales simultaneously, and any one tracer is affected mostly by those scales of the same size as the tracer cloud. In this theory, larger scales are more important at later times. However, we know that tracers were influenced by the large-scale convective structure from the very beginning because they were injected into existing updrafts and downdrafts. Convective structure memory appears to better explain the tracer dispersion that we observed here.

Although our results for short timesteps are similar to relative puff dispersion, most applications and parameterizations of transilient turbulence theory are for *absolute* dispersion (Sawford 1988; Stull 1988a), even at short timesteps. Namely, one desires a transilient matrix for short timesteps that, when reapplied many times during the course of a forecast, causes the same

dispersion and heat transport as a matrix for a larger timestep that "feels" the full effect of the instabilities and boundaries.

For mixed-layer simulation, we recommend that a matrix based on a timestep of one to two t_* (similar to those plotted in Fig. 5d, e, but without the numerical noise) be used as a "master" matrix, and that matrices for different timesteps be found as powers or roots of this master. Such a master and all of its powers or roots will always contain the desirable convective characteristics described in section 4a, and will provide the proper response to the imposed instabilities and boundary constraints. A proper simulation should also allow for the nonstationarity associated with real mixed layers. Similarly, any parameterization for the transilient matrices should include these larger-scale absolute dispersion effects, even for short timesteps.

6. Comparison with other concepts

a. Instantaneous vertical fluxes

The vertical profiles of instantaneous fluxes of each tracer at various times were calculated directly from the LES model. When these profiles are placed as columns side-by-side to form a matrix, and then contoured, the result is shown in Fig. 18. In these diagrams, each column represents the original source height of each tracer. For example, for the tracer emitted in the middle of the mixed layer ($z/z_i = 0.47$), we see at very short times (Fig. 18a) an upward (positive) flux above the emission height (i.e., at destinations greater than 0.47), and downward flux below that height, as expected for simple diffusion theory. At a time of $t/t_* = 4.0$ (Fig. 18f), there is virtually no net flux of the tracer emitted from the middle of the mixed layer, because that tracer is now almost uniformly mixed.

It would be expected that tracers emitted near the ground are the first to be drawn into the thermal updrafts, while emissions from middle and top of the mixed layer follow later. This is verified by the shift of the maximum positive flux region from the left side of Fig. 18c towards the right in Fig. 18d-f. Tracers that were emitted just below the top of the mixed layer ($z/z_i = 0.8$ or 0.9) are slowly carried downward in downdrafts and have a negative flux during most of the time, as shown in Fig. 18a-d. However, by $t/t_* = 4.0$, these tracers have a net upward (positive) flux, because they finally reach the surface where they are drawn into the base of thermals and rise. At this time there are negative fluxes associated with the entrainment down into the mixed layer from sources just above $z/z_i = 1.0$. These negative fluxes extend down to destination levels close to the ground.

b. Comparison with K-theory

In Fig. 18d-f, the regions of positive and negative flux cross the main diagonal. This would be impossible
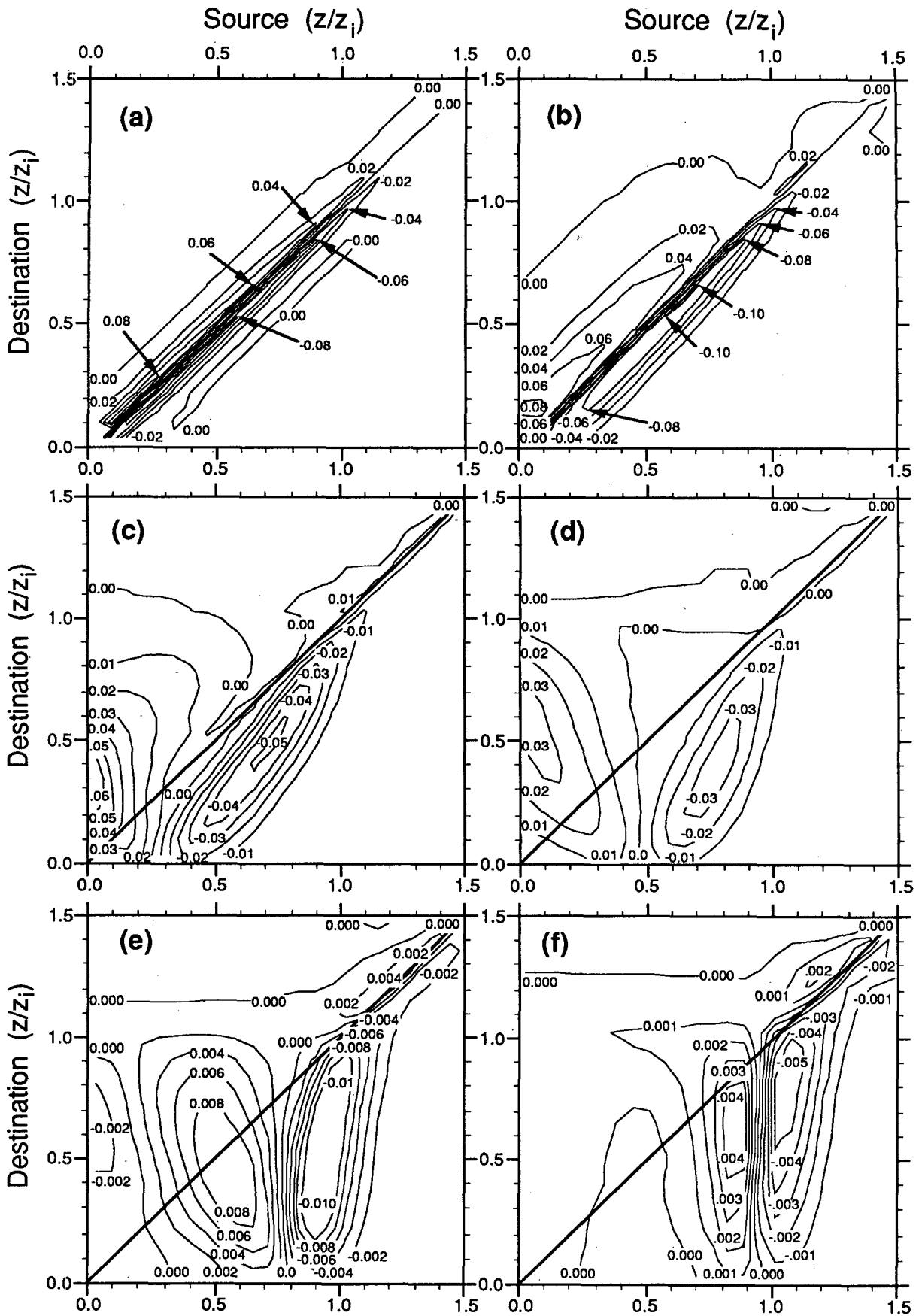
FIG. 18. Instantaneous flux of each tracer as a function of height, z/z_i, calculated directly from the LES model, at times t/t_* of: (a) 0.02, (b) 0.2, (c) 0.6, (d) 1.0, (e) 2.0, and (f) 4.0. Each tracer is represented by a different column in the contoured matrix, and is indexed by its original source height. The contoured fluxes are made dimensionless by dividing by w_*.

to model with a simple K-theory model (assuming positive K), which would instead cause a down-gradient diffusion similar to that plotted in Fig. 18a, spreading farther away from the main diagonal at later times.

If one uses the actual instantaneous local gradients and the actual fluxes to estimate K,

$$K_{ij}(\Delta t) = -\langle w\Psi_j \rangle_i \left/ \left(\frac{\partial \langle \Psi_j \rangle}{\partial z} \right)_i \right. \qquad (20)$$

the inadequacy of K-theory for convective mixed layers is apparent. Figure 19, for example, corresponds to time $t/t_* = 1.0$. First, we see that there are large regions of negative K (shaded), which implies countergradient diffusion. This, of course, is unrealistic and points to the inadequacy of K-theory, because the transport of tracer is governed by nonlocal large-eddy motions, not by local gradients.

Secondly, Fig. 19 shows regions of discontinuity, where unrealistically large negative K values are adjacent to large positive values. One region is in the lower left corner, and the other is along the line of dark shading going upward through the center of the diagram.

In an analog model of the same situation, this step would be even more dramatic, jumping from positive to negative infinity. In other regions indicated by the cross hatching in the diagram, both the flux and the gradient are so close to zero that K is undefined, or varies with apparently random positive and negative fluctuations (ill-defined).

Finally, and perhaps most importantly, we see that each different tracer (i.e., each column in the contoured matrix) has different profiles of K with height even though they are mixing in the same mixed layer. Thus, K is not a unique function of ambient turbulence intensity, but rather depends on the tracer source height and concentration. Hence parameterizations of K as a function of turbulence kinetic energy, Richardson number, stability, or other measures of the flow are inadequate for the convective mixed layer.

The theory of top-down/bottom-up diffusion (Wyngaard and Brost 1984) attempts to account for the variation of K with source height. However, as we see in Fig. 19 the small-eddy (gradient transport) diffusion from only top or bottom sources explain only a small portion of the complex K variations that occur
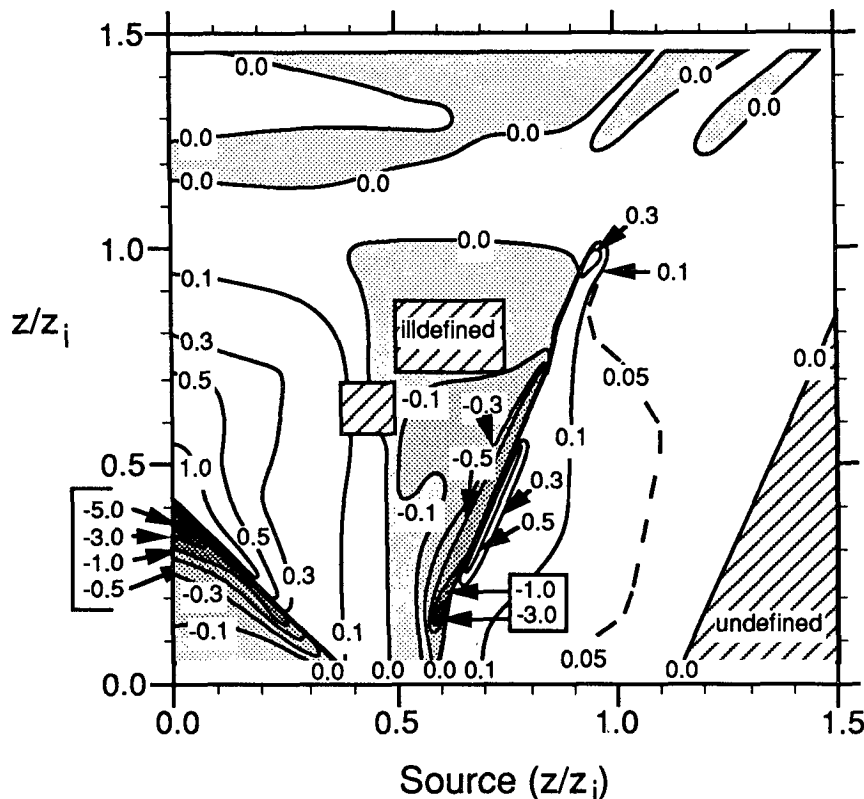

FIG. 19. Instantaneous value of eddy diffusivity (K) as a function of height, z/z_i, valid at t/t_* = 1.0, as calculated from the LES results by dividing the instantaneous flux (Fig. 18d) by the instantaneous gradient of tracer (Fig. 5d). Each column of the contoured matrix represents a different tracer. K is made dimensionless by dividing by $z_i w_*$. Negative values are shaded, and areas where K is undefined or ill-defined are indicated with cross-hatching.

throughout the mixed layer. We conclude that no form of small-eddy K-theory is adequate to describe the convective mixed layer, and we do not recommend its use in boundary layer, turbulence, and air pollution models for convective situations.

c. Vertical state Fourier spectrum of vertical velocity variance

The process spectrum (section 4g) represents the mixing due to vertical air motions of various sizes. Here we qualitatively compare $P_{k|m}$ with the state spectrum of vertical velocity in the vertical direction. (It is not appropriate to compare the process spectrum to the more common horizontal spectrum of w since the latter is more a measure of the width and spacing of thermals.) The vertical spectrum can be computed easily from individual columns of gridpoints in the fine grid LES vertical velocity field at $t = 0$. We limit the vertical domain to the 40 gridpoints within the CBL and entrainment zone ($0 \leq z \leq 1.25z_i$), and use a sine transform to obtain the spectral components. The sine transform assumes $w = 0$ at the top and bottom of the domain, which is generally valid. One must recognize that the profile is not periodic, leading to some difficulty in interpreting the spectrum. The spectrum of w is computed for each of the 25,600 vertical columns in the LES model, then averaged to get the mean vertical spectrum. We have also conditionally sampled the spectra according to whether the mean vertical velocity in a column was positive or negative, and averaged these separately to obtain mean spectra for updrafts and downdrafts. The resulting spectra are shown in Fig. 20.

The greatest spectral energy is associated with the lowest wavenumbers, or largest wavelengths, and decreases by three or four orders of magnitude for the smallest resolvable scales of motion. At the largest
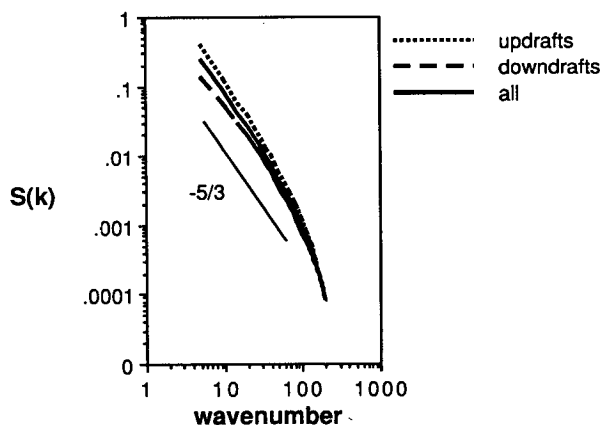

FIG. 20. Vertical spectrum of w normalized by $w_*^2 z_i$, vs wavenumber $k z_i$, computed from the LES vertical velocity field at t/t_* = 0.

wavelengths the variance of upward velocity is three times greater than the downward velocity variance. The curves converge at the smallest scales, where the variance is independent of whether w is positive or negative. The spectra appear to follow a $-\frac{5}{3}$ power relationship at the lower wavenumbers. At high wavenumbers a stronger decline is to be expected because of the filtering implied by the finite grid.

Both the state spectrum of w and the process spectrum give emphasis to the larger scales of motion. However, the variance in the state spectrum increases monotonically for increasing wavelength, while at $\Delta t / t_* = 4.0$, $P_{k|m}$ shows the greatest mixing associated with wavelengths of $0.5z_i$.

d. Heat fluxes

We have used (3) to compute fluxes of heat using the transilient coefficients, where the Ψ_j correspond to $\overline{T}_j / T_*$. We begin with the nondimensional temperature profile given by Schmidt and Schumann (1989) and add heat to the lowest layer ($j = 1$) according to the nondimensional heat equation,

$$\frac{\overline{T}_1}{T_*}(\Delta t) = \frac{\overline{T}_1}{T_*}(t = 0) + \frac{\langle wT \rangle}{Q_s} \frac{\Delta t}{\Delta z} \quad (21)$$

where the nondimensional surface heat flux, $\langle wT \rangle / Q_s \equiv 1$.

The resulting heat fluxes, $F_k^{\text{heat}}(\Delta t)$, evaluated according to Eq. (3), are shown in Fig. 21 for three time intervals. It is clear that for short and intermediate time intervals the transilient coefficients do not predict the correct heat flux. This is because the c_{ij} for short time-steps do not correctly represent the physics occurring in warm updrafts and cool downdrafts, as discussed in section 5. The agreement improves with increasing $\Delta t / t_*$ when the "memory" of the convective structures is incorporated into the transilient coefficients. The large errors near the top of the domain are a product of erroneous small-scale numerical diffusion.

Figure 22 shows profiles of the nondimensional net heat flux due to small (0–$0.12z/z_i$), medium (0.12–$0.44z/z_i$), and large (0.44–$1.5z/z_i$) eddies at $\Delta t/t_*$ = 4.0, computed by summing the heat transport spectrum over the appropriate eddy sizes. The net heat flux contribution from small eddies is negligible below the inversion except near the surface. The large values near the top of the domain are associated with large numerical errors. The medium scales contribute positively to the net heat flux in the lower CBL, as warm air is transported upward from the surface, and negatively to the net heat flux in the upper CBL and stable layer, due to entrainment of warmer air from the inversion layer. The component of the net heat flux associated with the large scales is out of phase with that of the medium scales. Maxima are found near the surface, just above the middle of the CBL, and at the inversion level, where the upward heat transport in thermals ris-
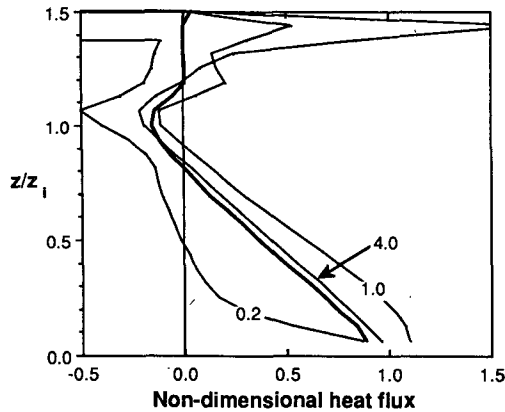
FIG. 21. Nondimensional heat flux, $F_k^{heat}(\Delta t)$, as a function of height, z/z_i for various time intervals, $\Delta t/t_*$. The actual heat flux from the LES calculation is given by the heavy solid line.

ing from the surface largely balances the negative small and medium-scale contributions associated with entrainment.

Using both aircraft turbulence measurements and LES results, Jochum (1988) computed vertical profiles of sensible heat flux for approximately the same size intervals as used here. However, her eddy size ranges were defined by horizontal wavelengths of state variables, while ours is a vertical wavelength or parcel displacement distance. She found nearly linear profiles for all size ranges. The smallest scales were important only near the surface. Below about $0.6z_i$ the strongest positive heat flux was due to the medium scales, while above that level the large eddies dominated. She also found the strongest negative heat flux associated primarily with medium scales below the inversion. Our results agree with those of Jochum (1988) for small-scale and total heat flux profiles, but the partitioning of medium and large-scale contributions differs significantly. This difference is related to the different ways of defining wavelengths.
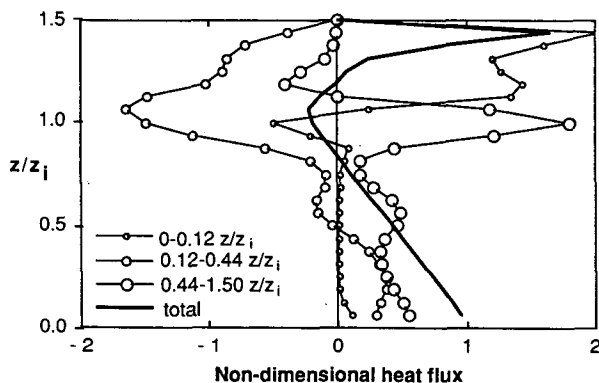
In Fig. 23 the heat flux is further partitioned into upward and downward components. This is accomplished by summing the heat transport spectrum over the appropriate eddy size ranges, where now $i > j$ for upward transport, and $i < j$ for downward transport. The net heat flux represents the balance of large upward and downward heat transports which are nearly equal and opposite. We note that this behavior is also seen in traditional time series (see, for example, Stull 1988c, p. 54). The smallest size range has very small values in the CBL and maximum values in the stable layer where the local temperature gradients (and numerical diffusion) are greatest. The medium, large, and total heat flux profiles have maxima near the middle of the CBL where the overall mixing is greatest, and minima near the surface and in the stable layer. In the CBL the downward and upward heat transports increase with increasing eddy size. This demonstrates that a small-eddy (K-theory) approximation misses most of the "action" in the CBL.

7. Summary and conclusions

Our goal was to measure nonlocal attributes of vertical mixing and convection in the atmospheric boundary layer. A three-dimensional large-eddy simulation model was used to forecast convection in an idealized windless mixed layer over a uniform surface with constant heat flux. Once the turbulence in the model had reached a quasi-steady state, a different passive tracer was injected into each of the 24 different grid layers of the model. Thus, each tracer served to mark a layer of source locations for air before being turbulently mixed into other layers.

At various times after tracer injection, the horizontally averaged fields of tracer concentrations were saved as a matrix, recording how much of each of the 24 tracers were found in each of the 24 grid layers. This matrix, called a transilient matrix, indicates the percentage of air in each of the destination layers that came from the various source layers during the time interval Δt since tracer injection.

The matrices describe the effects of all the resolvable

FIG. 22. Contributions to the vertical heat flux at $\Delta t/t_* = 4.0$ from small, medium, and large wavelength mixing processes.
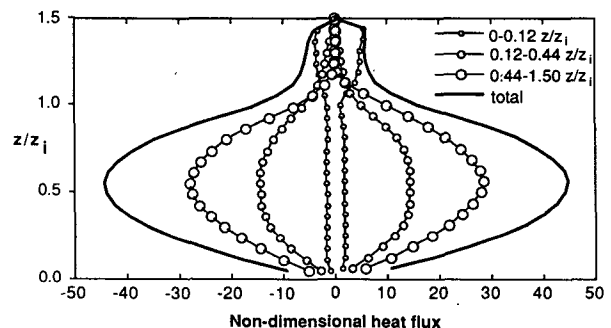

FIG. 23. As in Fig. 22, for upward and downward components of the vertical heat flux.

local and nonlocal vertical mixing processes. The distance of a matrix element from the main diagonal can be interpreted as a net transport distance or velocity, and the magnitude of the element indicates the relative amount of air undergoing that transport. For $\Delta t = 2t_*$ = 37 min we find that the matrix is asymmetric with a ridge of peak values on the downward side of the main diagonal, indicating a large amount of slow downward transport. There are small values at the origin, implying removal of most of the surface-layer air. The matrix has relative maxima at the ends of the cross-diagonal through the mixed layer, implying large-eddy convective overturning.

The time evolution of the transilient coefficients showed that the initial transport of tracers is downward from all levels except those nearest the surface. Air at the surface is transported rapidly to the upper half of the mixed layer. The actual vertical tracer flux was frequently counter to the local concentration gradient, implying that eddy diffusivity theory is inappropriate in this case.

Matrices for smaller time intervals are more symmetric, with more of the mixing occurring across shorter distances. Even when taken to an appropriate power to bring these matrices up to an effective time interval of $2t_*$, there is less large-eddy mixing than expected. This effect is related to the time dependence of the flux dynamics and the lack of convective structure "memory" that occurs when tracers are injected into preexisting convective elements.

To further analyze the matrices, a number of existing statistical descriptions were refined, and new techniques were developed. The equations for turbulent flux and for transport spectra (where the total turbulent flux of a scalar is partitioned by transport distance) at a given level were shown to depend on only the subset of air parcels crossing that level. An air mass transport spectrum equation was proposed that uses the difference in matrix elements across the main diagonal to highlight asymmetric mixing processes. A modification of the process spectrum equation was presented, which now correctly indicates the importance of various eddy sizes regardless of the amount of tracer that is transported.

The destination of a tracer from a single source height was tracked by isolating an individual column from the matrix and examining the evolution of that same column in matrices for different time intervals. Elements in any single column of the matrix can be used as weights to calculate the center of mass and concentration variance for tracers emitted from a single source height. Mixing length profiles were found by weighting the magnitudes of matrix elements by their distances from the main diagonal. A mixing intensity parameter based on the sum over matrix elements on opposite sides of the main diagonal is suggested as a way to measure overall turbulence vigor at a level. Another analysis approach is to partition the trans-

port into separate upward and downward components. Equations are given for the amount of air transported upward and downward away from any source, as well as corresponding equations for transport towards any destination. Separate mixing lengths are found for upward or downward transport, toward a destination or from a source, by weighting the distance from the main diagonal by the magnitude of each matrix element. The process spectrum definition is also examined in terms of upward versus downward contributions.

Results from these statistics reinforce traditional observations of turbulence state, and also provide additional insight into nonlocal transport. In the first category, the matrix asymmetry suggests a large amount of air moving slowly downward, and a smaller percentage of air moving rapidly upward, as expected with narrow updrafts and broad downdrafts. The transilient matrices exhibit a positive skewness of vertical mixing-process velocity in the mixed layer that becomes more pointed and symmetric near the top of the mixed layer. Vertical mixing intensity profiles are similar in shape to traditional vertical velocity-variance profiles, with peak magnitudes at about $\frac{1}{3}$ to $\frac{1}{2}$ of the mixed layer depth. The center of mass of a tracer inserted at the surface rises above the middle of the mixed layer before settling back to the middle, while for tracers originating near the top of the mixed layer the center of mass sinks below the middle of the mixed layer before returning to $0.5z_i$. The dispersion rate is initially greatest for tracers emitted near the middle of the mixed layer, but air from the surface experiences the greatest dispersion over intermediate time scales.

The air mass transport spectrum showed that negative (downward) net transport is associated with small vertical transport distances, while the larger vertical transport distances are associated with positive (upward) net transport, again reinforcing the concept of slow downdrafts and fast updrafts. Small eddies (or parcel transport across small distances) play a very minor role in the mixed layer heat flux, except near the surface and in the entrainment zone. Medium-size eddies cause most of the negative het flux in the entrainment zone, in spite of the positive flux contribution from the larger eddies that bring up warm air from the surface layer. K-theory has difficulties over much of the interior of the mixed layer.

In the second category of results are the many partitions of statistics with respect to upward and downward transport. This is similar to conditional sampling using vertical velocity, except that ours consider the actual transport across finite distances, while the vertical velocity gives no information on the actual net distances moved by the air parcels. The upward and downward contributions to heat flux are individually about 100 times greater than the net flux near the middle of the mixed layer, but are of opposite sign and nearly cancel each other. The large eddies contribute to about two-thirds of this directional flux, the medium

ones contribute about one-third, and small eddies contribute very little.

During a time interval of $\Delta t = t_*$, roughly 95% of the air is transported upward from near the surface, but from the middle of the mixed layer about 35% has gone up and 60% has gone down. From just below the entrainment zone, roughly 10% moves upward and 78% downward. The remaining air at those levels remains within the respective grid layers. Focusing on destinations instead of sources of air movement, we find that about 55% of the air arriving just below the entrainment zone came from below, while about 30% came from above, associated with entrainment. At the middle of the mixed layer approximately equal amounts came from below and above. The differences between the upward and downward transport, and between the transport toward or from a level, reflect the asymmetry of the mixing processes.

For short time intervals ($\Delta t/t_* \leqslant 0.2$), upward and downward mixing lengths have magnitudes of less than $0.2z_i$, reach their peak values within the bottom half of the mixed layer, and have roughly the same shape profiles regardless of direction. For time intervals greater than about $0.6t_*$, the mixing lengths approach 50% of the mixed layer depth, but the upward and downward curves are now substantially different. Close to the ground, the mixing length for air coming from or going towards the surface must by necessity be small because the eddies cannot go through the ground, but mixing to or from higher altitudes is associated with very large eddies. The opposite, of course, is true for air just below the capping inversion.

Process spectra measure the contributions to the mixing from every scale of the resolvable turbulence, regardless of the amount of scalar that is transported. For small time intervals the smaller size eddies dominate, while the medium-size eddies are the most important for time intervals greater than about $1.0t_*$. Furthermore, downward mixing is most vigorous at slightly smaller wavelengths than upward mixing within the top half of the mixed layer, but the opposite is true closer to the ground. After a long time period the net effects of upward and downward mixing processes are equivalent.

We compared the process spectra to Fourier spectra of vertical velocity computed from vertical columns of grid points in the LES. The peak in this spectrum occurs at the longest wavelengths, as is expected for thermals that fill the mixed layer. A $-\frac{5}{3}$ power relationship is also observed over a limited portion of the spectrum, also at the longest wavelengths.

We have attempted to demonstrate and explore the wealth of information that is contained within a transilient turbulence matrix. The transilient matrix was initially conceived as a first-order closure approximation, to forecast the effects of turbulence given knowledge of only the mean fields [Eq. (1)]. Although we presented numerical measurements of the transilient

matrix, a true first-order closure scheme requires a parameterization of the matrix based on the known mean fields of state variables such as temperature and wind.

It is still quite a challenge to develop such a parameterization. A useful parameterization should be responsive to changes in the mean field, and should work for unstable, neutral, stable, and cloud-topped boundary layers. It should also have the observed asymmetries for the unstable case, and should work for arbitrary (but reasonable) timesteps and grid spacings. The latter requires that the parameterization account for the flux dynamics and the convective structure memory in some way, in particular for small timesteps. In this regard we believe that the transilient matrix for $\Delta t/t_* \sim 1$ contains the essential physics of the mixing, and that matrices corresponding to smaller timesteps should be found as roots of this "master" matrix. The earlier parameterization suggested by Stull and Driedonks (1987) reduced a matrix of n^2 coefficients to a function of four parameters. It had some of the desired qualities, but it produced only symmetric matrices and did not account for the memory effect. Thus it was not able to capture some of the characteristics we have presented here.

APPENDIX A

Kinematic Flux Equation

Here we show that the flux at level k depends only on those eddies that cross level k. Starting with the kinematic flux equation,

$$F_k = \frac{\Delta z}{\Delta t} \sum_{i=1}^{k} \sum_{j=1}^{n} c_{ij}[\langle \Psi_i \rangle - \langle \Psi_j \rangle] \qquad (A1)$$

we split the j-sum into two parts: the sum from $j = 1$ to k, and the sum from $j = k + 1$ to n. The distributive law allows us to separate the first term, yielding:

$$F_k = \frac{\Delta z}{\Delta t} \left\{ \sum_{i=1}^{k} \left[\langle \Psi_i \rangle \sum_{j=1}^{k} c_{ij} \right] - \sum_{j=1}^{k} \left[\langle \Psi_j \rangle \sum_{i=1}^{k} c_{ij} \right] \right.$$

$$\left. + \sum_{i=1}^{k} \sum_{j=k+1}^{n} [c_{ij}\langle \Psi_i \rangle - c_{ij}\langle \Psi_j \rangle] \right\}$$

In the first two terms above, the $\langle \Psi_i \rangle$ was moved out of the j-sum, and the $\langle \Psi_j \rangle$ was moved out of the i-sum, because i and j are independent.

Because of mass and state continuity (Stull 1988c), the sum of c_{ij} over all rows and also over all columns

must equal unity individually. Thus, the sum of c_{ij} from 1 to k in both of the first two terms above can be replaced by one minus the sum from $k + 1$ to n. Next, in the second term only we switch the i and j indices, which we can do because i and j are arbitrary (dummy) indices. We then have

$$F_k = \frac{\Delta z}{\Delta t} \{ \sum_{i=1}^{k} \langle \Psi_i \rangle - \sum_{i=1}^{k} \sum_{j=k+1}^{n} c_{ij} \langle \Psi_i \rangle$$

$$- \sum_{i=1}^{k} \langle \Psi_i \rangle + \sum_{i=1}^{k} \sum_{j=k+1}^{n} c_{ji} \langle \Psi_i \rangle$$

$$+ \sum_{i=1}^{k} \sum_{j=k+1}^{n} c_{ij} \langle \Psi_i \rangle - \sum_{i=1}^{k} \sum_{j=k+1}^{n} c_{ij} \langle \Psi_j \rangle \}.$$

The first and third terms cancel, and the second and fifth terms cancel, giving an expression for the flux at level k that depends only on those eddies crossing that level:

$$F_k = \frac{\Delta z}{\Delta t} \sum_{i=1}^{k} \sum_{j=k+1}^{n} [c_{ji} \langle \Psi_i \rangle - c_{ij} \langle \Psi_j \rangle]. \quad \text{(A2)}$$

The first sum is over layers below the level k, and the second sum is over layers above k.

APPENDIX B

The Subgrid Scale Model

The subgrid scale (SGS) fluxes are approximated in terms of the resolved fields and the SGS kinetic energy $\overline{E''} \equiv \frac{1}{2} \overline{u_i''^2}$, for which we integrate the closed model equation

$$\frac{D\overline{E''}}{Dt} = -\overline{u_i'' u_j''} \frac{\partial \bar{u}_i}{\partial x_j} + \beta g \overline{w'' T''}$$

$$+ \frac{\partial}{\partial x_i} \left[\frac{5}{3} \mathcal{L} c_{3m} \overline{E''}^{1/2} \frac{\partial \overline{E''}}{\partial x_i} \right] - c_{\epsilon m} \frac{\overline{E''}^{3/2}}{\mathcal{L}} \quad \text{(B1)},$$

The turbulent heat, mass and momentum fluxes and their respective anisotropic components

$$\overline{A_{ij}''} = \overline{u_i'' u_j''} - \frac{2}{3} \delta_{ij} \overline{E''}, \quad \text{(B2)}$$

are determined from the following set of algebraically approximated second-order closure equations:

$$0 = -(1 - c_{Gm}) \frac{2}{3} \overline{E''} \left(\frac{\partial \bar{u}_i}{\partial x_j} + \frac{\partial \bar{u}_j}{\partial x_i} \right) + (1 - c_{Bm})$$

$$\times \left[\beta g \left(\delta_{i3} \overline{u_j'' T''} + \delta_{j3} \overline{u_i'' T''} - \frac{2}{3} \delta_{ij} \overline{u_3'' T''} \right) \right]$$

$$- c_{Rm} \frac{\overline{E''}^{1/2}}{\mathcal{L}} \overline{A_{ij}''} \quad \text{(B3)}$$

$$0 = -(1 - c_{GT}) \frac{2}{3} \overline{E''} \frac{\partial \bar{T}}{\partial x_i}$$

$$+ (1 - c_{BT}) \beta g \overline{T''^2} \delta_{i3} - c_{RT} \frac{\overline{E''}^{1/2}}{\mathcal{L}} \overline{u_i'' T''}, \quad \text{(B4)}$$

$$0 = -(1 - c_{G\Psi}) \frac{2}{3} \overline{E''} \frac{\partial \bar{\Psi}}{\partial x_i}$$

$$+ (1 - c_{B\Psi}) \beta g \overline{\Psi'' T''} \delta_{i3} - c_{R\Psi} \frac{\overline{E''}^{1/2}}{\mathcal{L}} \overline{u_i'' \Psi''}, \quad \text{(B5)}$$

$$0 = -2 \overline{u_j'' T''} \frac{\partial \bar{T}}{\partial x_j} - c_{\epsilon T} \frac{\overline{E''}^{1/2} \overline{T''^2}}{\mathcal{L}}, \quad \text{(B6)}$$

$$0 = -\overline{u_j'' \Psi''} \frac{\partial \bar{T}}{\partial x_j} - \overline{u_j'' T''} \frac{\partial \bar{\Psi}}{\partial x_j} - c_{\epsilon \Psi} \frac{\overline{E''}^{1/2} \overline{\Psi'' T''}}{\mathcal{L}}. \quad \text{(B7)}$$

This set of second-order closure equations is a straightforward extension of those given in Schmidt and Schumann (1989). It results from the more complete system deduced by Gibson and Launder (1976) by using arguments as given in Mellor and Yamada (1974), Sommeria (1976) and Schemm and Lipps (1976). In particular, it is assumed that local time derivatives, advective fluxes and anisotropic production rates contribute little to the anisotropic components of the fluxes. These approximations can be justified by scale analysis (Schemm and Lipps 1976). The vertical heat flux, the temperature variance, and the scalar-temperature covariance can be determined explicitly by solving the above linear system of equations. Using the abbreviations,

$$c_\gamma = \frac{2}{3} \frac{1 - c_{GT}}{c_{RT}}, \quad c_\Psi = \frac{2}{3} \frac{1 - c_{G\Psi}}{c_{R\Psi}}, \quad \text{(B8)}$$

$$G = \frac{2(1 - c_{BT})}{c_{RT} c_{\epsilon T}} \frac{\beta g \mathcal{L}^2}{\overline{E''}}, \quad G_\Psi = \frac{1 - c_{B\Psi}}{c_{R\Psi} c_{\epsilon \Psi}} \frac{\beta g \mathcal{L}^2}{\overline{E''}}, \quad \text{(B9)}$$

we obtain

$$\overline{T''^2} = 2 \frac{c_\gamma}{c_{\epsilon T}} \frac{\mathcal{L}^2}{1 + G(\partial \bar{T}/\partial z)} \left(\frac{\partial \bar{T}}{\partial x_i} \right)^2, \quad \text{(B10)}$$

$$\overline{\Psi'' T''} = \frac{1}{c_{\epsilon \Psi}} \frac{1}{1 + G_\Psi(\partial \bar{T}/\partial z)} \left[(c_\Psi + c_\gamma) \mathcal{L}^2 \frac{\partial \bar{\Psi}}{\partial x_j} \frac{\partial \bar{T}}{\partial x_j} \right.$$

$$\left. - \frac{c_\gamma G \mathcal{L}^2}{1 + G(\partial \bar{T}/\partial z)} \frac{\partial \bar{\Psi}}{\partial z} \left(\frac{\partial \bar{T}}{\partial x_i} \right)^2 \right]. \quad \text{(B11)}$$

In order to ensure finite positive solutions of $\bar{\Psi}$, we replace the expressions $\{1 + G \partial \bar{T}/\partial z\}$ and $\{1 + G_\Psi \partial \bar{T}/ \partial z\}$ by unity if they become less than one. This approach has also been used by Schemm and Lipps (1976). Moreover, we found it necessary to replace $(\partial \bar{\Psi}/\partial x_j)(\partial \bar{T}/\partial x_j)$ in (B11) by $(\partial \bar{\Psi}/\partial z)(\partial \bar{T}/\partial z)$ for strictly non-negative concentration values which are close to zero, because otherwise this term causes small

negative values of $\bar{\Psi}$. Once these covariances are computed, the flux components follow from equations (B3) to (B5).

The length scale, $\mathcal{L}$, is prescribed as a function of height z above the surface, and the average mesh spacing, Δ, by

$$\mathcal{L} = \min(\Delta, c_{\mathcal{L}}z), \quad \Delta = \frac{1}{3}(\Delta x + \Delta y + \Delta z). \quad (B12)$$

All essential model coefficients can be determined from the spectra of kinetic energy and temperature variance in the inertial–convective subrange of locally isotropic turbulence. In Appendix 2 of Schmidt and Schumann (1989), this is shown in detail for momentum and heat transfer. The corresponding coefficients for transport of passive scalars are set equal to those for heat transfer, which is appropriate because of the equality of the Kolmogorov constants for temperature and scalar spectra (Andreas 1987). The values of the coefficients are:

$$c_{\epsilon m} = 0.845, \quad c_{\epsilon T} = c_{\epsilon\Psi} = 2.02,$$

$$c_{Gm} = 0.55, \quad c_{Bm} = 0.55, \quad c_{GT} = c_{G\Psi} = 0.50,$$

$$c_{BT} = c_{B\Psi} = 0.50, \quad c_{Rm} = 3.50,$$

$$c_{RT} = c_{R\Psi} = 1.63, \quad c_{3m} = 0.20, \quad c_{\mathcal{L}} = c_{\epsilon m}.$$

APPENDIX C

Sensitivity to LES Specifications

The transilient coefficients were derived from the results of large eddy simulation, rather than directly from observations. As the LES results depend to some degree upon the grid resolution, subgrid scale turbulence parameterization, and other details of the model, we must determine to what extent the transilient coefficients also depend on those factors. Figure 24 compares the values of c_{ij}, $j = 1, 7, 15$, and 22, at $\Delta t / t_* = 1.0$ for four different versions of the coarse grid large eddy model, as well as the medium and fine grid versions. We note that the sensitivity of the coarse grid model to the model specifications is likely to be greater than that of the medium and fine resolution versions because of the greater impact of the changes on the finite difference errors.

1. Sensitivity to scalar-temperature covariance

In the scalar-temperature covariance equation (B11) the product of the three-dimensional gradients of $\bar{\Psi}$ and $\bar{T}$ contains the contributions from all three dimensions, and this is used in the reference case where the scalar reference level $\Psi_0 = 1000$ was large. For cases with zero reference level, we must approximate this product by omitting the lateral gradient contributions in order to ensure positive Ψ-solutions. We examine the sensitivity of the results to this approximation by omitting the lateral gradient contributions for fixed scalar reference level $\Psi_0 = 1000$. The dotted curve in Fig. 24a shows that the effect of this change is negligible everywhere except in the middle of the CBL for scalars originating immediately near the surface, and even here the error in c_{ij} is less than 20%. Therefore, we conclude that this approximation has no significant effect on the results.

2. Sensitivity to scalar reference level

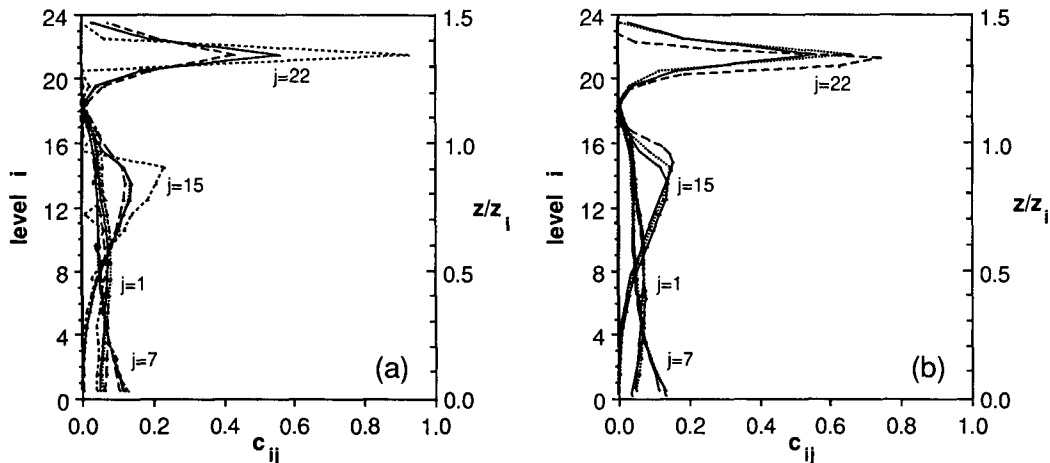As discussed in section 3b, the Smolarkiewicz (1984) differencing scheme used by the model is sensitive to

FIG. 24. Profiles of $c_{ij}(\Delta t)$, $j = 1, 7, 15$, and 22, at $\Delta t / t_* = 1.0$ for (a) coarse grid model (solid), and changes in the model parameterizations: the removal of $(\partial\bar{\Psi}/\partial x_j)(\partial\bar{T}/\partial x_j)$ ($j = 1, 2$) from the subgrid scale parameterization (dotted); setting the reference level $\Psi_0 = 0$ (long dashed); setting the reference level $\Psi_0 = 10\,000$ (dot-dashed); and setting $\overline{u_i''\Psi''} \equiv 0$ (short dashed); and (b) changes in grid resolution: coarse grid (dotted); medium grid (solid); and fine grid (long dashed).

the scalar reference level; thus a level of $\Psi_0 = 1000$ was added and later subtracted from the scalar concentrations to reduce numerical diffusion. The effect is illustrated by the dashed curve in Fig. 24a, in which this artificial addition and subtraction of 1000 was not performed. This run also neglected the lateral gradient product as described in the previous paragraph. The profiles of c_{ij} are smeared due to numerical diffusion, particularly near the inversion and in the stable layer. In another test the reference level was set to 10^4 to see whether the diffusion could be further reduced using a greater value. The dot-dashed curve corresponding to this test in Fig. 24a is coincident with the solid curve corresponding to $\Psi_0 = 1000$. Thus, the addition of a large reference value to the scalar concentrations is useful for reducing numerical diffusion, and $\Psi_0 = 1000$ is adequate to provide the maximum reduction of this diffusion.

3. Sensitivity to the subgrid scale parameterization

The subgrid scale (SGS) parameterization estimates the concentration fluxes for scales of motion which are too small to be explicitly resolved by the model. It is a source of diffusion, and acts to damp some of the fine-scale resolved concentration fluctuations. The SGS parameterization is more important in the coarse grid model than in the fine grid version, for which Schmidt and Schumann (1989) showed a negligible contribution of SGS processes to the vertical heat flux everywhere except near the surface (where the resolved vertical velocity is constrained to be zero), and near the inversion. We examined the importance of SGS processes by setting $\overline{u_i'' \Psi''} \equiv 0$ everywhere in the coarse grid model, as shown by the short-dashed curve in Fig. 24a. This intensifies the upward transport of surface air ($j = 1$) because the SGS diffusion causes slight downgradient transport while the large scale motions introduce countergradient transports. Some noise is seen in the profile corresponding to mid-CBL air ($j = 7$) which results from the lack of damping. The removal of SGS diffusion also reduces the downward transport of inversion level air ($j = 15$). In the stable layer the vertical diffusion of air is very small, as we expect it should be; this reflects the unrealistically large diffusion produced by the SGS parameterization in the stable layer. This suggests that in future simulations one should reduce the SGS mixing length l [see Eq. (B12)] in the stable layer as proposed by Moeng (1984).

4. Sensitivity to grid resolution

Figure 24b shows profiles of c_{ij} for simulations using the coarse, medium, and fine resolution versions of the model as described in section 3c. The differences between the results of the three simulations are small throughout the CBL, and slightly larger near the inversion and in the stable layer. In general, the higher

resolution simulations experience less diffusion than the lowest resolution case. This is because smaller eddies are explicitly resolved, reducing the proportion of the motion handles by the SGS parameterization with its associated excess diffusion. The qualitatively similar behavior of the coarse, medium, and fine resolution simulations justifies our selection of the "grid M" model as a compromise between accuracy and computational effort. We note that the offset of one grid level between the grid F peak and the grid C and grid M peaks is the result of an error in selecting the proper height interval for initialization of Ψ at this level, but this does not affect our conclusions regarding this experiment.

REFERENCES

Andreas, E. L., 1987: On the Kolmogorov constants for the temperature-humidity cospectrum and the refraction index spectrum. *J. Atmos. Sci.,* **44,** 2399–2406.

Bougeault, P., 1983: A non-reflective upper boundary condition for limited-height hydrostatic models. *Mon. Wea. Rev.,* **111,** 420–429.

Busse, F. H., 1978: Non-linear properties of thermal convection. *Rep. Prog. Phys.,* **41,** 1930–1967.

Chatfield, R. B., and R. A. Brost, 1987: A two-stream model of the vertical transport of trace species in the convective boundary layer. *J. Geophys. Res.,* **92**(D11), 13 263–13 276.

Chen, C., and W. R. Cotton, 1983: Numerical experiments with a one-dimensional higher order turbulence model: Simulation of the Wangara day 33 case. *Bound.-Layer Meteor.,* **25,** 375–404.

Deardorff, J. W., 1970: Convective velocity and temperature scales for the unstable planetary boundary layer and for Rayleigh convection. *J. Atmos. Sci.,* **27,** 1211–1213.

——, 1974: Three-dimensional numerical study of turbulence in an entraining mixed layer. *Bound.-Layer Meteor.,* **7,** 199–226.

Eberhard. W. L., W. R. Moninger and G. A. Briggs, 1988: Plume dispersion in the convective boundary layer. Part I: CONDORS field experiment and example measurements. *J. Appl. Meteor.,* **27,** 599–616.

Fiedler, B. H., and C.-H. Moeng, 1985: A practical integral closure model for mean vertical transport of a scalar in a convective boundary layer. *J. Atmos. Sci.,* **42,** 359–363.

Finger, J. E., and H. Schmidt, 1986: On the efficiency of higher order turbulence models simulating the convective boundary layer. *Beitr. Phys. Atmos.,* **59,** 505–517.

Gibson, M. M., and B. E. Launder, 1976: On the calculation of horizontal, turbulent, free shear flows under gravitational influence. *J. Heat Transfer,* **98**(C1), 81–87.

Greenhut, G. K., and S. J. S. Khalsa, 1987: Convective elements in the marine atmospheric boundary layer. Part I: Conditional sampling statistics. *J. Climate Appl. Meteor.,* **26,** 813–822.

Jochum, A. M., 1988: Turbulent transport in the convective boundary layer over complex terrain. Preprints, *Eighth Symp. on Turbulence and Diffusion,* San Diego, Amer. Meteor. Soc., 417–420.

Klemp, J. B., and D. R. Durran, 1983: An upper boundary condition permitting internal gravity wave radiation in numerical mesoscale models. *Mon. Wea. Rev.,* **111,** 430–444.

Lamb, R. G., 1978: A numerical simulation of dispersion from an elevated point source in the convective planetary boundary layer. *Atmos. Environ.,* **12,** 1297–1304.

Mason, P. J., and D. J. Thompson, 1987: Large eddy simulations of neutral-static-stability planetary boundary layer. *Quart. J. Roy. Meteor. Soc.,* **113,** 413–443.

Mellor, G. L., and T. Yamada, 1974: A hierarchy of turbulence closure models for planetary boundary layers. *J. Atmos. Sci.,* **31,** 1791–1806; Corrigenda 1977, *J. Atmos. Sci.,* **34,** 1482.

Moeng, C.-H., 1984: A large-eddy simulation model for the study of planetary boundary layer turbulence. *J. Atmos. Sci.,* **41,** 2052–2062.

——, and J. C. Wyngaard, 1984: Statistics of conservative scalars in the convective boundary layer. *J. Atmos. Sci.,* **41,** 3161–3169.

Nieuwstadt, F. T. M., and J. P. J. M. M. de Valk, 1987: A large eddy simulation of buoyant and non-buoyant plume dispersion in the atmospheric boundary layer. *Atmos. Environ.,* **21,** 2573–2787.

Sawford, B. L., 1988: Comments on "Transilient turbulence theory." Part I and III. *J. Atmos. Sci.,* **45,** 2092–2093.

Schemm, C. E., and F. B. Lipps, 1976: Some results of a simplified three-dimensional numerical model of atmospheric turbulence. *J. Atmos. Sci.,* **33,** 1021–1041.

Schmidt, H., 1988: Grobstruktur-Simulation konvektiver Grenzschichten. Ph.D. thesis, Ludwig-Maximilians-Universität, München, DFVLR-FB 88-30, 134 pp. [Available from DLR, 5000 Köln 90, Federal Republic of Germany.]

——, and U. Schumann, 1989: Coherent structure of the convective boundary layer derived from large-eddy simulations. *J. Fluid Mech.,* in press.

Schumann, U., 1989: Large-eddy simulation of turbulent diffusion with chemical reactions in the convective boundary layer. *Atmos. Environ.,* in press.

——, T. Hauf, H. Höller, H. Schmidt and H. Volkert, 1987: A mesoscale model for the simulation of turbulence, clouds and flow over mountains: Formulation and validation examples. *Beitr. Phys. Atmos.,* **60,** 413–446.

Smolarkiewicz, P. K., 1984: A fully multidimensional positive definite advection transport algorithm with small implicit diffusion. *J. Comput. Phys.,* **54,** 325–362.

——, and T. L. Clark, 1986: The multidimensional positive definite advection transport algorithm: Further development and applications. *J. Comput. Phys.,* **67,** 396–438.

Sommeria, G., 1976: Three-dimensional simulation of turbulent processes in an undisturbed trade wind boundary layer. *J. Atmos. Sci.,* **33,** 216–241.

Stull, R. B., 1984: Transilient turbulence theory. Part I: The concept of eddy mixing across finite distances. *J. Atmos. Sci.,* **41,** 3351–3367.

——, 1986: Transilient turbulence theory. Part III: Bulk dispersion rate and numerical stability. *J. Atmos. Sci.,* **43,** 50–57.

——, 1988a: A reevaluation of two dispersion theories. *J. Atmos. Sci.,* **45,** 2082–2091.

——, 1988b: Pollutant dispersion and mixed-layer modeling using asymmetric transilient matrices. Preprints, *Eighth Symp. on Turbulence and Diffusion,* San Diego, Amer. Meteor. Soc., 263–266.

——, 1988c: *An Introduction to Boundary Layer Meteorology.* Kluwer, 666 pp.

——, 1988d: Process spectra: The spectra of turbulent processes rather than turbulence states. Preprints, *Eighth Symp. on Turbulence and Diffusion,* San Diego, Amer. Meteor. Soc., 88–91.

——, and T. Hasagawa, 1984: Transilient turbulence theory. Part II: Turbulent adjustment. *J. Atmos. Sci.,* **41,** 3368–3379.

——, and A. G. M. Driedonks, 1987: Applications of the transilient turbulence parameterization to atmospheric boundary layer simulations. *Bound.-Layer Meteor.,* **40,** 209–239.

Sun, W.-Y., and C.-Z. Chang, 1986: Diffusion model for a convective layer. Part II: Plume released from a continuous point source. *J. Climate Appl. Meteor.,* **25,** 1454–1463.

Willis, G. E., and J. W. Deardorff, 1975: A parameterization of diffusion into the mixed layer. *J. Appl. Meteor.,* **14,** 1451–1458.

——, and ——, 1976: A laboratory model of diffusion into the convective planetary boundary layer. *Quart. J. Roy. Meteor. Soc.,* **102,** 427–445.

——, and ——, 1978: A laboratory study of dispersion from an elevated source within a modeled convective planetary boundary layer. *Atmos. Environ.,* **12,** 1305–1311.

——, and ——, 1981: A laboratory study of dispersion from a source in the middle of the convectively mixed layer. *Atmos. Environ.,* **15,** 109–117.

Wyngaard, J. C., and R. A. Brost, 1984: Top-down bottom-up diffusion of a scaler in a convective boundary layer. *J. Atmos. Sci.,* **41,** 102–112.

Young, G. S., 1988: Turbulence structure of the convective boundary layer. Part II. Phoenix 78 aircraft observations of thermals and their environment. *J. Atmos. Sci.,* **45,** 727–735.

Zeman, O., and J. L. Lumley, 1976: Modeling buoyancy driven mixed layers. *J. Atmos. Sci.,* **33,** 1974–1988.